



Non-linear stabilization of high-order Flux Reconstruction schemes via Fourier-spectral filtering



Kartikey Asthana^{*,1}, Manuel R. López-Morales¹, Antony Jameson²

Department of Aeronautics and Astronautics, Stanford University, CA 94305, USA

ARTICLE INFO

Article history:

Received 11 January 2015
 Received in revised form 6 June 2015
 Accepted 21 September 2015
 Available online 8 October 2015

Keywords:

High-order
 Flux Reconstruction
 Shock capturing
 Stabilization
 Filter
 Discontinuous Galerkin

ABSTRACT

High-order Flux Reconstruction (FR) schemes have been limited in their application to transonic and supersonic problems on account of numerical instabilities related to the resolution of jump discontinuities. These instabilities arise from aliasing errors associated with the collocation projection of the flux corresponding to the numerical solution onto the polynomial basis of the numerical flux. In this paper, we obtain energy bounds on the numerical solution via FR to prove that stability can be ensured for any polynomial order by the addition of adequate artificial dissipation such that the solution is energy-stable beyond a critical grid resolution. This artificial viscosity is then approximately posed as a Fourier filtering operation which is implemented in the physical space via a strictly local convolution integral. The filter is selectively applied to ‘troubled’ cells as indicated by a discontinuity sensor based on the spectral concentration method. Numerous numerical tests in 1-D and 2-D have been performed. The proposed approach captures shock discontinuities while preserving accuracy in smooth regions of the solution, even for very high polynomial orders such as $P = 119$. The filtered solution provides reduced total variation, reduced maximum overshoot/undershoot, and even allows sub-element shocks to be localized in the interior of an element.

© 2015 Elsevier Inc. All rights reserved.

1. Introduction

The last two decades have devoted significant attention to discontinuous finite element methods as efficient tools for solving hyperbolic conservation laws. These methods combine the ability of continuous finite element schemes to refine the order of approximation of the solution polynomial while retaining localized stencils similar to finite volume schemes. In particular, discontinuous Galerkin (DG) schemes [1–3] have emerged as a popular option for obtaining high-order solutions of fluid flows on complex geometries amenable only to unstructured grids. In the case of linear fluxes, stability can be proven [4] by showing that the L_2 norm of the numerical solution remains bounded for consistent choices of the interface flux. However, for a general non-linear flux, stability of the numerical solution cannot be guaranteed, especially if the governing equations admit a solution with jump discontinuities. One possible strategy to handle such cases is to use a deformable mesh in conjunction with adaptive finite element algorithms [5–7]. While these algorithms appear to be robust for the reported simulations of 2-D and 3-D Euler equations [8], there is no rigorous assurance of stability. The alternative

* Corresponding author. Tel.: +1 202 740 2474.

E-mail addresses: kasthana@stanford.edu (K. Asthana), mlopez14@stanford.edu (M.R. López-Morales), jameson@baboon.stanford.edu (A. Jameson).

¹ PhD candidate, Stanford University.

² Professor, Department of Aeronautics and Astronautics, Stanford University.

strategy to tackle non-linear fluxes involves the intelligent addition of artificial dissipation and encompasses a variety of different approaches.

The simultaneous requirements of stability and accuracy naturally fork two approaches. The first one suggests the addition of a variable amount of dissipation in the entire domain. An instance of this approach is the use of limiters [9–13]. The idea was initially proposed in the context of finite volume schemes to capture shock discontinuities in supersonic inviscid fluid flow [9]. The action of the limiter is to detect local extrema and limit their growth by comparing the solution/derivative in an element with the range of solution/derivative values in the neighboring elements. Hierarchical limiting strategies [11,12] have been proposed more recently where derivatives are progressively limited, and it has been argued that the limited solution retains the highest possible accuracy. However, such limiting procedures are sensitive to the order and extent of limiting and may require special treatment to handle negative pressure values for the Euler equations. Additionally, the repeated action of the limiter can lead to diffusion of sharp features that would not have necessarily resulted in shocks.

Another instance of this approach is the incorporation of an explicit filtering operation applied periodically to dampen high frequency components that would potentially result in numerical instabilities. High-order finite difference compact schemes have been used in conjunction with anti-aliasing filters [14,15] to suppress instabilities arising from mesh non-uniformity. The action of such filters is similar to that of low pass filters used in Large Eddy Simulation [16–18] which serve as a sink of energy for parts of the wavenumber spectrum that cannot be accurately resolved. Filters designed explicitly for shock-capturing have been proposed [19–21] as well. In the case of finite element schemes, spectral viscosity can be added in the Fourier space [22] or a convenient Jacobi space such as those of Legendre polynomials [23,24]. Such spectral viscosity can be equivalently posed as the spectral expansion of differential operators in the physical space [25]. These approaches benefit from rigorous studies [26–28] which prove that multiplication with an appropriate filter kernel can accelerate the convergence of Fourier expansions of piecewise discontinuous functions. Note that the use of periodic filtering, where the filter is applied after every few timesteps, differs from the approach where filtering is used once as a post-processing operation [29] to reduce errors and improve convergence.

The other approach towards adding artificial dissipation proceeds by first detecting numerical instabilities through a sensor and then selectively attending to troubled elements [30]. The detection of discontinuities partially relieves the subsequent filtering or limiting action from the constraints of preserving order of accuracy, as smooth regions of the solution remain unchanged. Detectors have been proposed that utilize super-convergence of discontinuous Galerkin methods at the outflow boundaries of elements [31], or the expected rate of decay of modal coefficients in Legendre expansions [32]. The treatment of troubled cells on structured and unstructured grids has been carried out through WENO reconstruction [34,35] of the solution polynomial using the neighboring polynomials, or through the explicit addition of artificial viscosity [32,33] in the physical space. The addition of artificial diffusivity for shock capturing has also been proposed for high-order finite difference schemes [36,37].

In regard to flow physics, a consistent shock capturing scheme must not only satisfy the weak form of the conservation equation, but also respect entropy behavior dictated by the second law of thermodynamics. Entropy conservative as well as entropy stable second-order finite difference approximations have been derived by Tadmor for both semi-discrete [38] and fully-discrete [39] representations. Such entropy stability theory can be used to distinguish between shock discontinuities and rarefaction waves within a single computational cell. Non-linear entropy stability can be ensured for higher order difference schemes [40] through addition of suitable diffusion operators. More recently, entropy stable ENO schemes [41] as well as arbitrary order spectral collocation schemes [42] have also been obtained that provide entropy stability of the compressible Navier Stokes equations.

In this paper, we study the non-linear stability properties of the Flux Reconstruction [43–45] formulation which provides a unified formulation for recovering the collocation based nodal DG method, the Spectral Difference (SD) method [46,47] as well as providing scope for the prescription of schemes with reduced dispersion and dissipation errors [48] and schemes with continuous derivatives at the interfaces [49]. FR schemes benefit from solving the governing equation in strong form leading to a diagonal mass matrix. As in the case of DG, the FR formulation has been proven to be stable for linear fluxes for specific choices of the correction function leading to the development of the Energy Stable FR (ESFR) schemes [50]. However, for non-linear fluxes, Jameson et al. [52] have suggested that such ESFR schemes may be unstable on account of aliasing errors resulting out of the collocation projection of the flux onto the Lagrangian basis of the numerical flux.

In the present work, we build upon the result of Jameson et al. [52] to obtain energy bounds for the numerical solution via FR and show that aliasing errors may not vanish even in the asymptotic limit on polynomial order if the analytical flux function is not sufficiently smooth. We then prove that the addition of adequate artificial dissipation can ensure non-linear stability for any polynomial order. We pose this addition of artificial viscosity as a Fourier filtering operation which is implemented in the physical space via convolution. A notable departure from previous filtering strategies is in the incorporation of edge information from neighboring elements in order to control inter-element discontinuities. Moreover, the filter is selectively applied to troubled cells as indicated by a sensor based on the concentration method [55,56]. Numerous numerical tests have been performed to validate the theoretical results.

The paper is formatted as follows. Sections 2 and 3 are concerned with the theoretical aspects of non-linear stability, including energy bounds on the numerical solution for a general flux and sufficient conditions for stability through addition of artificial dissipation. Section 4 describes the formulation of convolution filters in 1-D and 2-D on tensor product elements. Section 5 provides a brief overview of the concentration sensor used for detecting discontinuities. Finally, in Sections 6 and 7, we demonstrate the performance of the sensor and filter in several test cases: linear advection, Burger's equation,

Sod’s shock-tube, Shu–Osher shock-disturbance interaction [35], rigid body rotation, symmetric Riemann problem and the double Mach reflection case of Woodward and Colella [58].

2. Energy bounds for the numerical solution of non-linear scalar conservation laws via FR

We begin with a brief description of a general nodal discontinuous finite element scheme. While the numerical results for the present investigation utilize the Flux Reconstruction (FR) framework, the sensing and filtering formulations can be readily applied to other frameworks as well. Consider the 1-D scalar conservation law

$$\begin{aligned} \frac{\partial u}{\partial t} + \frac{\partial f(u)}{\partial x} &= 0, \quad x \text{ in } \Omega \in \mathbb{R}, t > 0, \\ u(x, 0) &= u_0(x). \end{aligned} \tag{1}$$

Assume the boundary conditions to be periodic for convenience. For a general discontinuous finite element scheme, the domain Ω is partitioned into N elements, $\Omega = \bigcup_{n=0}^{N-1} \Omega_n$, of variable width $h_n = x_{n+1} - x_n$ and each element is further discretized with $P + 1$ variably distributed solution points. For nodal methods, the discontinuous solution and flux can be defined as interpolating polynomials in the n th element,

$$\begin{aligned} u_n^\delta(x) &= \sum_{p=1}^{P+1} u_{n,p}^\delta l_{n,p}(x), \\ f_n^\delta(x) &= \sum_{p=1}^{P+1} f(u_{n,p}^\delta) l_{n,p}(x), \end{aligned} \tag{2}$$

where $l_{n,p}$ is the p th Lagrange polynomial in the n th element, and the superscript δ denotes a numerically evaluated quantity. Both u_n^δ and f_n^δ vanish outside the n th element. Introduce a linear isoparametric map from the physical domain $x \in \Omega_n = [x_n, x_{n+1}]$ to the parent domain $\xi \in [-1, 1]$ as

$$\xi|_{\Omega_n}(x) = 2 \frac{x - x_n}{x_{n+1} - x_n} - 1. \tag{3}$$

A detailed account of the FR framework can be found in [43]. Schemes belonging to the FR formulation can be parameterized by the choice of (i) solution points, (ii) flux correction function, and (iii) interface flux function which is often dictated by the physics of the underlying problem. In the case of linear fluxes, the choice of solution points only affects the interpolation error associated with the collocation projection of the initial condition onto the polynomial space of the solution [48], and does not alter the stability or accuracy properties [43]. Vincent et al. [50] have shown that linearly stable schemes can be obtained for a one-parameter family of flux-correction functions for which the broken Sobolev type norm defined as

$$|u^\delta|_{\Omega^\delta, (P,0)} = \left[\sum_{n=0}^{N-1} \int_{x_n}^{x_{n+1}} (u_n^\delta)^2 + \frac{c}{2} (J_n)^{2P} \left(\frac{\partial^P u_n^\delta}{\partial x^P} \right)^2 dx \right]^{1/2} \tag{4}$$

decays monotonically under exact time-integration. Here, $J_n = h_n/2$ denotes the Jacobian of the transformation defined in Eqn. (3) and the notation $|\mu|_{\Omega^\delta, q} = \left[\sum_{n=0}^{N-1} \int_{x_n}^{x_{n+1}} \left(\frac{\partial^q \mu_n}{\partial x^q} \right)^2 dx \right]^{1/2}$ denotes the q th Sobolev semi-norm of the piecewise defined function $\mu(x)$ over the numerical domain Ω^δ . Hence, the broken Sobolev norm in Eqn. (4) is indeed a weighted sum of the 0th and P th Sobolev semi-norms. The same authors have also demonstrated [51] using an eigenvalue computation that these schemes retain linear stability under numerical time integration when using standard three-stage, third-order (RK33) and four-stage, fourth-order (RK44) Runge–Kutta methods for non-vanishing CFL numbers that depend on P . However, in the more general case of non-linear fluxes, Jameson et al. [52] have shown that the growth rate of the norm in Eqn. (4) is dependent on aliasing errors and can no longer be guaranteed to decay with time. In particular,

$$\begin{aligned} \frac{1}{2} \frac{d}{dt} |u^\delta|_{\Omega^\delta, (P,0)}^2 &= \Theta + \sum_{n=0}^{N-1} \int_{\Omega_n} (f_n^\delta - f(u_n^\delta)) \frac{\partial u_n^\delta}{\partial x} dx \\ &\leq \sum_{n=0}^{N-1} \int_{\Omega_n} (f_n^\delta - f(u_n^\delta)) \frac{\partial u_n^\delta}{\partial x} dx, \end{aligned} \tag{5}$$

since Θ is provably non-positive. The bounding terms in Eqn. (5), referred to as ‘aliasing errors’, are associated with the collocation projection of the non-linear flux corresponding to the numerical solution, $f(u_n^\delta)$, onto the polynomial space of the numerical flux, f_n^δ . This further emphasizes the choice of solution points, and the authors suggest the use of Gauss–Legendre quadrature points to reduce aliasing driven instabilities. In this section, we establish an upper bound on the rate of growth of the energy norm to show that aliasing errors may not vanish even in the asymptotic limit on polynomial order if the analytical flux function is not sufficiently smooth. This prepares us for Section 3 where we show that Fourier filtering can be sufficiently employed to ensure that the norm strictly decays for any polynomial order.

Define $\partial\Omega_n = \{x_n, x_{n+1}\}$ and let $\Omega^\delta = \bigcup_{n=0}^{N-1} (\Omega_n - \partial\Omega_n)$ denote the discrete domain obtained by removing the interface points from the physical domain. Similarly the numerical solution, numerical flux and the non-linear flux corresponding to the numerical solution can be denoted by the piecewise sums $u^\delta = \sum_{n=0}^{N-1} u_n^\delta$, $f^\delta = \sum_{n=0}^{N-1} f_n^\delta(x)$, and $\tilde{f} = \sum_{n=0}^{N-1} f(u_n^\delta)$ respectively. The broken integral in Eqn. (5) can then be rewritten as

$$\frac{1}{2} \frac{d}{dt} |u^\delta|_{\Omega^\delta, (P,0)}^2 \leq \int_{\Omega^\delta} (f^\delta - \tilde{f}) \frac{\partial u^\delta}{\partial x} dx = \int_{\Omega^\delta} (I_P(\tilde{f}) - \tilde{f}) \frac{\partial u^\delta}{\partial x} dx, \tag{6}$$

where I_P denotes the piecewise collocation projector,

$$I_P(\tilde{f}(x)|_{\Omega_n}) = \sum_{p=1}^{P+1} \tilde{f}(x_{n,p}) l_{n,p}(x) = \sum_{p=1}^{P+1} f(u_{n,p}^\delta) l_{n,p}(x) = f_n^\delta(x), \tag{7}$$

and $x_{n,p}$ denotes the p th solution point in the n th element. Since the sign of right hand side in Eqn. (6) cannot be determined *a-priori*, we are interested in establishing an upper bound for its magnitude. Using the Cauchy–Schwarz inequality, we get

$$\begin{aligned} \int_{\Omega^\delta} (I_P(\tilde{f}) - \tilde{f}) \frac{\partial u^\delta}{\partial x} dx &\leq \left[\int_{\Omega^\delta} (I_P(\tilde{f}) - \tilde{f})^2 dx \int_{\Omega^\delta} \left(\frac{\partial u^\delta}{\partial x} \right)^2 dx \right]^{1/2} \\ &= \|I_P(\tilde{f}) - \tilde{f}\|_{\Omega^\delta, 0} \left\| \frac{\partial u^\delta}{\partial x} \right\|_{\Omega^\delta, 0}, \end{aligned} \tag{8}$$

where $\|\cdot\|_{\Omega^\delta, q}$ denotes the q th Sobolev norm over Ω^δ .

Let $\tilde{f} \in H^{q_f}(\Omega_n)$, $q_f \geq 0$ for $n = 0, 1, \dots, N - 1$, where H denotes the standard Sobolev space. Then, by results from approximation theory [4,59,60] on the error bound for collocation projection onto Gauss–Legendre points, we get

$$\|I_P(\tilde{f}) - \tilde{f}\|_{\Omega^\delta, 0} \leq C_1 h^\sigma \left\| \frac{\partial^\sigma \tilde{f}}{\partial x^\sigma} \right\|_{\Omega^\delta, 0}, \tag{9}$$

where $\sigma = \min(P + 1, q_f)$, $h = \max_{n=0}^{N-1} (h_n)$, and C_1 is merely some constant. Substituting Eqns. (8), (9) into Eqn. (6), we obtain an upper bound for the broken norm of the numerical solution

$$\frac{1}{2} \frac{d}{dt} |u^\delta|_{\Omega^\delta, (P,0)}^2 \leq C_1 h^\sigma \left\| \frac{\partial^\sigma \tilde{f}}{\partial x^\sigma} \right\|_{\Omega^\delta, 0} \left\| \frac{\partial u^\delta}{\partial x} \right\|_{\Omega^\delta, 0}. \tag{10}$$

In the special case of $P = 0$, $\frac{\partial u^\delta}{\partial x} \equiv 0$ over Ω^δ which verifies the expectation that the first order scheme is non-linearly stable.

For the general case of $P \geq 1$, if \tilde{f} is smooth, $q_f \rightarrow \infty$, and therefore $\sigma \rightarrow P + 1$. Then, Eqn. (10) suggests that the growth term is bounded by the usual interpolation errors $\sim h^{P+1} \|\tilde{f}^{(P+1)}\|$. Consequently, the bound vanishes in the limit of $P \rightarrow \infty$ or $h \rightarrow 0$ and non-linear stability would be guaranteed.

However, when \tilde{f} has a discontinuous derivative such that σ is independent of P , the convergence of the bound to zero cannot be achieved in the limit of $P \rightarrow \infty$. This suggests that aliasing errors may not vanish at all for $P \geq 1$ unless dissipation is artificially introduced into the conservation law.

3. Non-linear stabilization of the numerical solution via Fourier-spectral filtering

Following the conclusions from Section 2, we now describe a mechanism for adding artificial dissipation to suppress non-linear instabilities driven by aliasing errors. The treatment contained herein borrows from the spectral viscosity method

[22,23] in that artificial dissipation is essentially introduced in Fourier space. However, instead of applying an explicit filter onto the Fourier coefficients, the filtering operator is cast as a convolution in physical space similar to deconvolution strategies [18,19,21] used in Large Eddy Simulation. This circumvents the computational complexity involved in performing Fourier transforms of piecewise polynomial functions.

Note that viscosity can be introduced in the Jacobi-spectral space as well [24,25,28,32,61]. While such an approach is convenient, as spectral expansions in orthogonal polynomial bases are computationally efficient and well-conditioned, it amounts to a purely local filtering operation where the solution in each element is filtered independent of that in the neighbors. On the other hand, the use of a convolution integral automatically leads to a coupling between neighboring elements. Such coupling has been shown to perform favorably in the case of WENO [30] based limiting strategies for discontinuous Galerkin methods.

Similar to the approach in classical finite volume schemes, we begin by introducing a series of artificial diffusion terms in Eqn. (1) such that the numerical conservation law is given by

$$\frac{\partial u^\delta}{\partial t} + \frac{\partial I_P(\tilde{f})}{\partial x} = \sum_{s=1}^{\infty} (-1)^{s+1} \epsilon_s \frac{\partial^{2s} u^\delta}{\partial x^{2s}}, \tag{11}$$

where non-vanishing terms in the summation are obtained for $s \leq P/2$ for even P , and for $s \leq (P - 1)/2$ for odd P . Let the infinite sum in the artificial diffusion term be denoted by \mathcal{A}_n in the n th element. The corresponding contribution to the bound in Eqn. (6) can be obtained by evaluating $\sum_{n=0}^{N-1} \int_{x_n}^{x_{n+1}} (u^\delta \mathcal{A}_n + \frac{c}{2} (J_n)^{2P} \frac{\partial^P u^\delta}{\partial x^P} \frac{\partial^P \mathcal{A}_n}{\partial x^P}) dx$. However, $\frac{\partial^P \mathcal{A}_n}{\partial x^P}$ vanishes identically as u_n^δ is a polynomial of degree P . Hence, the artificial dissipation term results into the new energy bound

$$\frac{1}{2} \frac{d}{dt} |u^\delta|_{\Omega^\delta, (P,0)}^2 \leq \int_{\Omega^\delta} (I_P(\tilde{f}) - \tilde{f}) \frac{\partial u^\delta}{\partial x} dx + \sum_{s=1}^{\infty} \int_{\Omega^\delta} (-1)^{s+1} \epsilon_s u^\delta \frac{\partial^{2s} u^\delta}{\partial x^{2s}} dx. \tag{12}$$

For the artificial component, integrating by parts the s th term, s times, and using the periodicity of boundary conditions we get

$$\int_{\Omega^\delta} (-1)^{s+1} u^\delta \frac{\partial^{2s} u^\delta}{\partial x^{2s}} dx = - \left\| \frac{\partial^s u^\delta}{\partial x^s} \right\|_{\Omega^\delta, 0}^2. \tag{13}$$

Summing over the series and substituting into Eqn. (12), we finally obtain

$$\frac{1}{2} \frac{d |u^\delta|_{\Omega^\delta, (P,0)}^2}{dt} \leq C_1 h^\sigma \left\| \frac{\partial^\sigma \tilde{f}}{\partial x^\sigma} \right\|_{\Omega^\delta, 0} \left\| \frac{\partial u^\delta}{\partial x} \right\|_{\Omega^\delta, 0} - \sum_{s=1}^{\infty} \epsilon_s \left\| \frac{\partial^s u^\delta}{\partial x^s} \right\|_{\Omega^\delta, 0}^2. \tag{14}$$

The direct addition of artificial dissipation into the hyperbolic system introduces additional restrictions on the CFL limit which might be significant in boundary layer meshes. Additionally, in the particular case of FR, the calculation of several higher order derivatives increases computational complexity and effort by a significant factor. Therefore, it is expedient to add dissipation through integral operators instead. A convenient option is to pose the dissipation in the Fourier-spectral space and apply it in the physical space via a convolution integral. This can be achieved by first time-splitting Eq. (11) into natural and artificial terms [28,60] so that a first order approximation in time can be written as

$$\hat{u}^\delta(x, t + \Delta t) = u^\delta(x, t) - \int_t^{t+\Delta t} \frac{\partial I_P(\tilde{f})}{\partial x}(x, \tau) d\tau, \tag{15}$$

$$u^\delta(x, t + \Delta t) = \hat{u}^\delta(x, t + \Delta t) + \int_t^{t+\Delta t} \sum_{s=1}^{\infty} (-1)^{s+1} \epsilon_s \frac{\partial^{2s} u^\delta}{\partial x^{2s}}(x, \tau) d\tau. \tag{16}$$

Hence, the addition of artificial dissipation can be regarded as the update for the parabolic equation given by

$$\frac{\partial u^\delta}{\partial t} = \sum_{s=1}^{\infty} (-1)^{s+1} \epsilon_s \frac{\partial^{2s} u^\delta}{\partial x^{2s}}. \tag{17}$$

Substituting u^δ by its spatial Fourier transform $u^\delta = \int_{-\infty}^{\infty} U^\delta(k, t) \exp(ikx) dk$ into Eqn. (17) expands the derivative operators in spectral space,

$$\frac{\partial}{\partial t} \int_{-\infty}^{\infty} U^\delta(k, t) \exp(ikx) dk = \sum_{s=1}^{\infty} (-1)^{s+1} \epsilon_s \int_{-\infty}^{\infty} (ik)^{2s} U^\delta(k, t) \exp(ikx) dk, \tag{18}$$

which yields the ordinary differential equation for the evolution of the Fourier coefficient as a function of wavenumber k ,

$$\frac{dU^\delta(k, t)}{dt} = \sum_{s=1}^{\infty} (-1)^{s+1} \epsilon_s (ik)^{2s} U^\delta(k, t). \tag{19}$$

A first order approximation of the time derivative in Eqn. (19) confirms that the addition of artificial dissipation in physical space is equivalent to a filtering operation in Fourier space,

$$\bar{V}(k, t) = \left(1 + \sum_{s=1}^{\infty} (\epsilon_s \Delta t) (-1)^{2s+1} k^{2s} \right) U^\delta(k, t), \tag{20}$$

where $\bar{V}(k)$ denotes the Fourier coefficients of the filtered numerical solution. The transfer function of the filter can therefore be written as

$$G(k) = 1 - \sum_{s=1}^{\infty} \alpha_s k^{2s}, \tag{21}$$

where $\alpha_s = \epsilon_s \Delta t$.

The stabilizing effect of artificial dissipation can now be observed by considering the severe case where the flux corresponding to the numerical solution does not have continuous derivatives. This has been expressed succinctly in the following results.

Theorem 3.1. Given $u^\delta(x)$, $f^\delta(x)$ defined as in Eqn. (2), $f(u^\delta(x)) \in H^1(\Omega_n)$ for $n = 0, 1, \dots, N - 1$, the numerical solution for the scalar conservation law in Eqn. (11) by an FR scheme of polynomial order P is monotonically decreasing on the norm in Eqn. (4) in either asymptotic limit $h \rightarrow 0$ or $P \rightarrow \infty$ if

$$\epsilon_1 > 0, \epsilon_j \geq 0 \text{ for } j = 2, \dots, P; \tag{22}$$

$$\epsilon_1 \propto \frac{h^a (P + 1)^b}{\Delta t_{\text{CFL}}}, \quad a < 2, b > -1, \tag{23}$$

where Δt_{CFL} denotes the maximum time step for linear stability for the chosen time stepping scheme.

Proof. In the case of $f(u^\delta(x)) \in H^1(\Omega_n)$, Eq. (14) reduces to

$$\frac{1}{2} \frac{d}{dt} |u^\delta|_{\Omega^\delta, (P,0)}^2 \leq C_1 h \left\| \frac{\partial \tilde{f}}{\partial x} \right\|_{\Omega^\delta, 0} \left\| \frac{\partial u^\delta}{\partial x} \right\|_{\Omega^\delta, 0} - \sum_{s=1}^{\infty} \epsilon_s \left\| \frac{\partial^s u^\delta}{\partial x^s} \right\|_{\Omega^\delta, 0}^2.$$

Using $\epsilon_j \geq 0$ for $j = 2, \dots, P$,

$$\begin{aligned} \frac{1}{2} \frac{d}{dt} |u^\delta|_{\Omega^\delta, (P,0)}^2 &\leq C_1 h \left\| \frac{d\tilde{f}}{du^\delta} \frac{\partial u^\delta}{\partial x} \right\|_{\Omega^\delta, 0} \left\| \frac{\partial u^\delta}{\partial x} \right\|_{\Omega^\delta, 0} - \epsilon_1 \left\| \frac{\partial u^\delta}{\partial x} \right\|_{\Omega^\delta, 0}^2, \\ &\leq C_1 h \|w^\delta\|_{\Omega^\delta, 0} \left\| \frac{\partial u^\delta}{\partial x} \right\|_{\Omega^\delta, 0}^2 - \epsilon_1 \left\| \frac{\partial u^\delta}{\partial x} \right\|_{\Omega^\delta, 0}^2, \\ &\leq C_1 h |\Omega|^{1/2} w_{\text{max}}^\delta \left\| \frac{\partial u^\delta}{\partial x} \right\|_{\Omega^\delta, 0}^2 - \epsilon_1 \left\| \frac{\partial u^\delta}{\partial x} \right\|_{\Omega^\delta, 0}^2, \end{aligned}$$

where $w^\delta(x)$ denotes the numerical wavespeed, w_{max}^δ denotes the maximum numerical wavespeed in the domain and we have used $\|w\|_{\Omega^\delta, 0} \leq \sqrt{|\Omega|} w_{\text{max}}^\delta$. The CFL restriction on the time-step requires

$$\Delta t \leq \Delta t_{\text{CFL}} = C_2 \frac{h}{w_{\text{max}}^\delta (P + 1)}, \tag{24}$$

where $C_2 \sim \mathcal{O}(1)$ is only weakly dependent on P . Writing $\alpha_1 = \epsilon_1 \Delta t$, we get

$$\frac{1}{2} \frac{d}{dt} |u^\delta|_{\Omega^\delta, (P,0)}^2 \leq h w_{\text{max}}^\delta \left\| \frac{\partial u^\delta}{\partial x} \right\|_{\Omega^\delta, 0}^2 \left(C_1 |\Omega|^{1/2} - \alpha_1 C_2^{-1} \zeta^{-1} (P + 1) h^{-2} \right), \tag{25}$$

where $\zeta = \Delta t / \Delta t_{\text{CFL}}$. This suggests that the artificial dissipation term dominates the right hand side with respect to convergence in grid spacing $h \rightarrow 0$ as well as polynomial order $P \rightarrow \infty$, provided that $\alpha_1 > 0$ and

$$\alpha_1 \propto \zeta h^a (P + 1)^b, \quad a < 2, b > -1. \tag{26}$$

Noting that $\epsilon_1 = \frac{\alpha_1}{\Delta t} \propto \frac{h^a (P+1)^b}{\Delta t_{\text{CFL}}}$ completes the proof. \square

Theorem 3.1 deals with stability in the asymptotic limit of polynomial order $P \rightarrow \infty$. It provides the rate of growth of diffusion coefficients with h and P .

Theorem 3.2. Under the conditions specified by Eqns. (22), (23), $\exists h_{\text{crit}}(P)$ such that the numerical solution of Eqn. (11) by an FR scheme of polynomial order P is monotonically decreasing on the norm in Eqn. (4) for any $h < h_{\text{crit}} \sim (P + 1)^{\frac{b+1}{2-a}}$.

Proof. Admitting $\alpha_1 = C_3 \zeta h^a (P + 1)^b$ into Eqn. (25) yields

$$\frac{1}{2} \frac{d}{dt} |u^\delta|_{\Omega^\delta, (P,0)}^2 \leq h w_{\text{max}}^\delta \left\| \frac{\partial u^\delta}{\partial x} \right\|_{\Omega^\delta, 0}^2 \left(C_1 |\Omega|^{1/2} - C_2^{-1} C_3 h^{a-2} (P + 1)^{b+1} \right).$$

Hence, $\frac{1}{2} \frac{d}{dt} |u^\delta|_{\Omega^\delta, (P,0)}^2 \leq 0$ for $h < h_{\text{crit}}$ where

$$\begin{aligned} h_{\text{crit}} &= \left(\frac{C_3 (P + 1)^{b+1}}{C_1 C_2 |\Omega|^{1/2}} \right)^{\frac{1}{2-a}} \\ &= C_4 (P + 1)^{\frac{b+1}{2-a}}. \quad \square \end{aligned} \tag{27}$$

Theorem 3.2 deals with stability for a given polynomial order. It links the magnitude of the dissipation terms with a critical grid resolution. The constant C_2 can be determined from numerical eigenvalue computation of the CFL number for a given time integration scheme [48,51]. However, the constant C_1 is not directly available. Thus, h_{crit} cannot be determined exactly. However, this result shows that an unstable numerical solution can be stabilized by either increasing the strength of filtering or decreasing the grid spacing. We also see that the critical grid size, h_{crit} , increases with increasing polynomial order.

At this point, it is important to mention that we intend to use such filters that provide stability coupled with a robust discontinuity detector described in Section 5. This differs from the rigorous treatment in prior studies [24,26,27] wherein the filter is applied uniformly leading to certain additional constraints on the kernel required for conserving order of accuracy.

The conditions in **Theorem 3.1** are sufficient but not necessary for stability. We now explore a set of alternative conditions for suitability of filter kernels in Fourier space. These conditions are less restrictive in that the coefficients of higher order derivatives, $\alpha_i, i > 1$, can assume negative values as well. We begin by observing the effect of the filtering procedure on the numerical wave properties. Sengupta et al. [15] have shown that the application of an explicit filter modifies the numerical amplification factor A of the fully discretized differential equation,

$$A_{\text{eff}}(k^*, \zeta) = A(k^*, \zeta) G(k^*), \tag{28}$$

where $k^* = kh / (P + 1)$ is the non-dimensional wavenumber, $\zeta = \Delta t / \Delta t_{\text{CFL}}$ is the non-dimensional timestep, and A_{eff} is the modified amplification factor. The amplitude of A_{eff} is directly affected by the filter as $|A_{\text{eff}}| = |A| |G|$. Moreover, if $G(k^*)$ is complex, it can lead to modification of the numerical phase and group velocity as well, which can possibly worsen numerical dispersion. Hence we are interested in purely real, non-negative filter kernels bounded above by 1 for the entire range of resolvable wavenumbers,

$$0 \leq G(k^*) \leq 1, \quad \text{for } k^* \leq \pi. \tag{29}$$

Additionally, it is desirable to have minimal modification of low wavenumber components. This is satisfied by Eqn. (21) implicitly in the limit of $k^* \rightarrow 0$ as

$$\frac{d^s G}{dk^{*s}}(k^* = 0) = 0, \quad s = 0, 1. \tag{30}$$

Note that it is not necessary for the kernel to vanish at the Nyquist limit.

4. Formulation of convolution filters

As mentioned in Section 3, we can avoid the computational complexity involved in performing Fourier transforms of piecewise polynomial functions by casting Fourier-filtering as an integral operation. Taking transforms of both sides in Eqn. (20) and using the Convolution Theorem, we get

$$\bar{v}(x) = (u * g)(x) = \int_{-\infty}^{\infty} u^\delta(\xi)g(x - \xi)d\xi, \tag{31}$$

where $g(x) = \mathcal{F}^{-1}(G(k))$ is the inverse Fourier transform of the filter kernel.

Note that if the series in Eq. (21) is truncated at any level S , i.e. $\alpha_s = 0, s > S$, then $\mathcal{F}^{-1}(G(k)) = \delta(x) - \sum_{s=1}^S \alpha_s (-1)^{s+1} \delta^{(2s)}(x) / \pi^{2s}$ where $\delta(x)$ is the Dirac-delta function, and the purpose of casting the artificial dissipation term as a convolution would be defeated. Hence, we are interested in an infinite, convergent series that conforms to the requirements enlisted in the previous section and has an explicit inverse transform.

These constraints can be satisfied by well known filters such as the Gaussian, box, sharp-spectral and cosine filters. For instance, by choosing

$$\alpha_s = (-1)^{s+1} \frac{\Delta^{2s}}{2^s s!}, \tag{32}$$

we get

$$G(k; \Delta) = \exp\left(-\frac{k^2 \Delta^2}{2}\right) = \exp\left(-\frac{k^{*2} \Delta^{*2}}{2}\right), \tag{33}$$

where $\Delta^* = \Delta(P + 1)/h$ denotes the non-dimensional filter width and $k^* = kh/(P + 1)$ is the non-dimensional wavenumber. In this case,

$$g(x; \Delta) = \frac{1}{\sqrt{2\pi} \Delta^2} \exp\left(-\frac{x^2}{2\Delta^2}\right), \tag{34}$$

which we recognize as the standard Gaussian filter. Conventionally, the filter width is fixed by requiring that $G(k^* = \pi) = 0$. However, this would lead to a very dissipative filter kernel that significantly modifies a large portion of the spectrum. Instead, we can use Eqn. (32) to choose Δ from Eqn. (23), which for $a = 2, b = -1/2$ gives

$$\Delta = \gamma \left(\frac{\Delta t}{\Delta t_{\text{CFL}}}\right)^{1/2} \frac{h}{(P + 1)^{1/4}}, \tag{35}$$

for some constant γ which parameterizes the family of filters. The choice of $a = 2$ ensures that the filter width Δ depends linearly on the grid spacing h . This results in significant computational efficiency since, as shown in Section 4.1, such dependence in turn leads to a constant filter width $\hat{\Delta}$ in the parent space.

Similarly, we can obtain the box filter by choosing

$$G(k; \Delta) = \frac{\sin(k\Delta)}{k\Delta}, \tag{36}$$

$$g(x; \Delta) = \frac{1}{\Delta} \mathbb{I}_{[-\frac{\Delta}{2}, \frac{\Delta}{2}]}(x), \tag{37}$$

where \mathbb{I} denotes the indicator function. In this case, the kernel positivity requirement, Eqn. (29), restricts the range of admissible filter widths or equivalently the filter width parameter γ ,

$$\Delta \in \left[0, \frac{h}{P + 1}\right], \quad \gamma \in \left[0, \frac{1}{(P + 1)^{3/4}} \left(\frac{\Delta t_{\text{CFL}}}{\Delta t}\right)^{1/2}\right]. \tag{38}$$

The dependence of filter width on element size in Eqn. (35) implies that the filtering operator would need to be defined for every single element. For large meshes, this could lead to severe memory requirements. For this purpose, we are specifically interested in kernels that scale inversely with respect to coordinate scaling,

$$g(\phi x; \phi \Delta) = \frac{1}{\phi} g(x; \Delta). \tag{39}$$

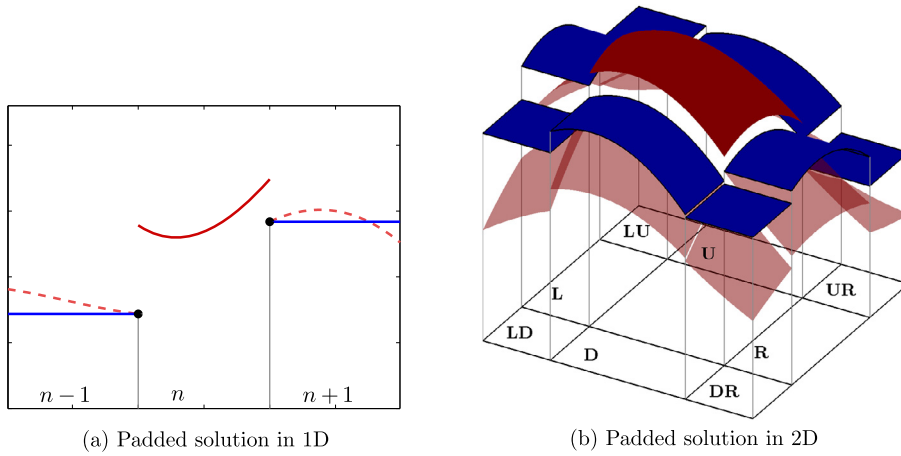


Fig. 1. Local representation of the piecewise solution obtained by padding interface-information from neighboring elements. The dashed curves/translucent surfaces represent the original piecewise solution; the solid lines/solid surfaces denote the padded solution.

4.1. Local filter formulation in 1-D

The convolution integral in Eqn. (31) stretches over the entire real line and a direct evaluation would require the global piecewise definition of u^δ . While such global filtering operations are performed for finite difference methods on structured meshes, they would lead to excessive computational cost and complexity in the case of unstructured meshes. In the discussion that follows, we propose an approximate local description of the filtering operation that accounts for the inter-element discontinuities and can be posed as a simple matrix-vector product. We begin by defining an operator \mathcal{P} that pads the piecewise polynomial solution in the parent space $\hat{u}^\delta(r)$ with the edge values of the neighboring elements,

$$\begin{aligned} \hat{v}_n(r) &= \mathcal{P}(\hat{u}^\delta(r)) \\ &= \hat{u}_n^\delta(r)\mathbb{I}_{(-1,1)}(r) + \hat{u}_{n-1}^\delta(1)\mathbb{I}_{(-\infty,-1]}(r) + \hat{u}_{n+1}^\delta(-1)\mathbb{I}_{[1,\infty)}(r), \end{aligned} \tag{40}$$

shown schematically in Fig. 1(a). The motivation behind the padding procedure is essentially heuristic and attempts to generate a local representation of both intra and inter element discontinuities. The filtered function can now be easily expressed via the convolution as

$$\tilde{v}_n(r) = \int_{-\infty}^{\infty} \hat{v}_n(\eta)g(x(r) - x(\eta); \Delta)J_n d\eta, \tag{41}$$

which can be simplified using Eqn. (39) to absorb the grid Jacobian and obtain a uniform filtering operator,

$$\begin{aligned} \tilde{v}_n(r) &= \int_{-\infty}^{\infty} \hat{v}_n(\eta)g(r - \eta; \Delta J_n^{-1})d\eta \\ &= \int_{-1}^1 \hat{u}_n^\delta(\eta)g(r - \eta; \hat{\Delta})d\eta + \hat{u}_{n-1}^\delta(1) \int_{-\infty}^{-1} g(r - \eta; \hat{\Delta})d\eta + \hat{u}_{n+1}^\delta(-1) \int_1^{\infty} g(r - \eta; \hat{\Delta})d\eta \\ &= \sum_{p=1}^{P+1} \hat{u}_{n,p}^\delta \int_{-1}^1 l_p(\eta)g(r - \eta; \hat{\Delta})d\eta + \hat{u}_{n-1}^\delta(1) \int_{-\infty}^{-1} g(r - \eta; \hat{\Delta})d\eta + \hat{u}_{n+1}^\delta(-1) \int_1^{\infty} g(r - \eta; \hat{\Delta})d\eta \\ &= \sum_{p=1}^{P+1} \hat{u}_{n,p}^\delta w_p(r) + \hat{u}_{n-1}^\delta(1)w_0(r) + \hat{u}_{n+1}^\delta(-1)w_{P+2}(r), \end{aligned} \tag{42}$$

where $\hat{\Delta} = \Delta J_n^{-1} = \left(\frac{\Delta t}{\Delta t_{CFL}}\right)^{1/2} \frac{2\gamma}{(P+1)^{1/4}}$ is the constant filter width in the parent domain and

$$w_p(r) = \int_{-1}^1 l_p(\eta)g(r - \eta, \hat{\Delta})d\eta \text{ for } 1 \leq p \leq P + 1,$$

$$\begin{aligned}
 w_0(r) &= \int_{-\infty}^{-1} g(r - \eta, \hat{\Delta}) d\eta = \int_{1+r}^{\infty} g(\eta, \hat{\Delta}) d\eta, \\
 w_{P+2}(r) &= \int_1^{\infty} g(r - \eta, \hat{\Delta}) d\eta = \int_{-\infty}^{r-1} g(\eta, \hat{\Delta}) d\eta.
 \end{aligned}
 \tag{43}$$

Since the value of the filtered solution is required only at the solution points r_q for $q = 1, 2, \dots, P + 1$, this procedure can be conveniently expressed as a matrix-vector product,

$$\hat{\mathbf{u}} = \mathbf{F}\hat{\mathbf{v}},
 \tag{44}$$

where \mathbf{F} is the filter matrix of dimensions $(P + 1) \times (P + 3)$ such that

$$F_{q,p} = w_p(r_q) \text{ for } 0 \leq p \leq P + 2, 1 \leq q \leq P,
 \tag{45}$$

and the vector of padded solution values is given by

$$\hat{v}_p = \begin{cases} u_{n,p}^\delta & 1 \leq p \leq P + 1 \\ u_{n-1}^\delta(1) & p = 0 \\ u_{n+1}^\delta(-1) & p = P + 2 \end{cases}
 \tag{46}$$

From an implementation point of view, the integrals in Eqn. (43), can be computed using adaptive quadrature or a quadrature rule of sufficiently high order. For simple filter kernels, the boundary terms, w_0 and w_{P+2} , can be computed analytically. Note that such numerical integration only needs to be performed once to compute the filter matrix \mathbf{F} , i.e. \mathbf{F} can be computed to arbitrary precision and stored thereafter.

Remark. As mentioned in Section 3, the act of explicitly filtering in spectral space using an element-local approximation of Eqn. (31) helps us to avoid the computational complexity involved in calculating several higher-order derivatives present in the artificial dissipation sum, Eqn. (11), and in circumventing additional restrictions imposed through the CFL requirement for such terms. However, these benefits come at the cost of possibly sacrificing the non-linear stability guaranteed by Theorems 3.1 and 3.2. A more careful analysis would be needed to design local filters that guarantee stability, perhaps in a weaker, element-local definition of solution energy. Another effect of such a choice is in regard to the conservation of numerical fluxes. Each action of filtering in the spectral space modifies the spectral data of the filtered variable depending on the form of the transfer function, Eqn. (21). Therefore, physical quantities would not be explicitly conserved across a filtering operation. However, the numerical conservation law is still integrated in time using the underlying FR scheme which is conservative by definition [43]. Therefore, the reconstructed flux is still conserved across elements.

4.2. Local filter formulation in 2-D

Local filtering operators can be constructed in multiple dimensions by extending the procedure outlined in the previous subsection. In the case of tensor product elements, filtering can be readily performed along lines in the square parent domain. However, such an action would introduce anisotropy as the information along diagonals would be ignored and the choice of axial directions would become important. An isotropic filtering operator can be obtained by considering multi-dimensional extensions of the procedure suggested in the previous subsection. As an example, Appendix A provides details for the case of tensor product elements.

5. Shock detection via the concentration method

This section briefly outlines the concentration method proposed by Gelb and Tadmor [53,54] and further refined by Gelb and Cates [55] towards the recovery of edges in piecewise smooth functions with finitely many jump discontinuities. While prior applications of this method have mostly been concerned with image processing and post-processing of numerical solutions to differential equations, Sheshadri and Jameson [56] have recently applied it to detect shock discontinuities in transonic, inviscid as well as viscous fluid flow. In the discussion that follows, we describe a simplified version of the concentration method which is obtained by fixing all but one of the parameters in the generalized formulation.

Consider the spectral projection of a piecewise smooth function $f : (x \in [-1, 1]) \rightarrow \mathbb{R}$ into the space of the first $P + 1$ Legendre polynomials,

$$S_P(f) = \sum_{k=0}^P \hat{f}_k L_k(x),
 \tag{47}$$

where $L_k(x)$ is the k th normalized orthogonal polynomial defined on the standard inner product and

$$\hat{f}_k = \int_{-1}^1 f(x)L_k(x)dx = \frac{-1}{k(k+1)} \int_{-1}^1 f(x) \frac{d}{dx} \left((1-x^2) \frac{dL_k}{dx} \right) dx, \tag{48}$$

where (\prime) denotes a derivative with respect to x . For simplicity, let f have a single jump-discontinuity at $x = c$, $[f](c) = f(c^+) - f(c^-)$. Then, integrating Eqn. (48) by parts and simplifying using properties of Legendre polynomials, we get

$$\hat{f}_k = \frac{-1}{k(k+1)} [f](c)(1-c^2)L'_k(c) + \mathcal{O}\left(\frac{-1}{k^2(k+1)^2}\right). \tag{49}$$

The first step in the concentration method is the localization of the projection in Eqn. (47) to the neighborhood of the jump using an appropriate concentration kernel. Towards this end, define the conjugate sum,

$$K_P * f(x) \equiv \frac{\pi \sqrt{1-x^2}}{P} \sum_{k=1}^P \hat{f}_k \frac{dL_k}{dx}. \tag{50}$$

Eqn. (49) can be used to show [54] that,

$$|K_P * f(x) - [f](x)| \leq \beta \frac{\log P}{P(1-x^2)^{1/4}}, \tag{51}$$

for $x \in \left(-1 + \frac{\beta}{P^2}, 1 - \frac{\beta}{P^2}\right)$ and some constant β . This suggests that for smooth pieces of the polynomial, the conjugate sum in Eqn. (50) converges to zero, and, if a jump discontinuity exists for points away from the boundaries $\{-1, 1\}$ of the domain, the sum converges to the magnitude of the jump at the rate of $\mathcal{O}\left(\frac{\log P}{P}\right)$. However, for discontinuous finite element schemes with polynomial order P , such convergence would be slow even for high orders. The separation of scales can be further increased through a non-linear enhancement

$$P(K_P * f(x))^2 \sim \begin{cases} \frac{(\log P)^2}{P} & \text{at a smooth point} \\ P[f]^2(x) & \text{at a discontinuity} \end{cases} \tag{52}$$

This effectively exponentiates the relative convergence term by a power of two. A sharper separation can be achieved by choosing higher powers during the enhancement. Finally, for moderately large P , an accurate and reliable shock sensor can be defined as

$$\theta(x; J) = \begin{cases} 1 & P(K_P * f(x))^2 > J \\ 0 & \text{otherwise} \end{cases} \tag{53}$$

In general, the value of the enhanced kernel in Eqn. (52) increases with polynomial order, magnitude of the discontinuity, and proximity of the discontinuity from the boundaries of the bi-unit domain. This behavior has been portrayed in Table 1 which records the maximum value of the enhanced kernel for a centered step, $\text{sgn}(x)$, a skewed step, $\text{sgn}(x - 1/2)$, a C_0 kink, $x_+ = \max(x, 0)$, and a C_1 kink, $\cos(3 + 1.3 \sin(x))$. We see that for high polynomial orders, $P \geq 5$, the concentration method clearly demarcates discontinuities in the function's value from those in the function's derivatives.

These observations certainly provide for an *a-posteriori* procedure of fixing the sensor threshold by observing the sensor values for a few initial time steps and manually selecting a suitable threshold. However, a practical choice is to select the average of the maximum values for the cases of a centered step and a C_0 kink. In other words, the sensor detects a discontinuity for normalized polynomials that are sharper than the shape midway between a centered step and a ramp.

It is important to mention that the use of the above procedure for shock detection requires appropriate normalization of the solution polynomial $u(x)$. This can be expressed as

$$U(x) = \frac{u(x) - u_{\min}}{u_{\max} - u_{\min} + \epsilon}, \tag{54}$$

where ϵ represents the tolerance at machine precision. For conservation laws with linear fluxes, it suffices to take the maximum and minimum values of the solution over the entire domain. However, for non-linear problems, especially those comprising multiple shocks of different strengths, it is important to normalize the solution in each element with respect to its local extrema.

Table 1

Maximum value of the enhanced kernel in Eqn. (52) over the solution points in $[-1, 1]$. The functions are normalized with respect to the extrema over the point values.

P	C_1 kink $\cos(3 + 1.3 \sin(x))$	C_0 kink $x_+ = \max(x, 0)$	Centered step $\text{sgn}(x)$	Skewed step $\text{sgn}(x - 1/2)$
5	1.7701	1.2536	3.6493	5.3244
6	1.5959	1.9925	3.5958	6.4424
7	1.4084	1.0910	4.5360	5.5975
8	1.1411	1.5527	4.6109	6.4980
9	1.0572	0.9366	5.4535	7.3697
10	1.0019	1.2722	5.6066	7.0400

6. Numerical results in 1-D

This section demonstrates the performance of the convolution filtering approach along with the concentration based discontinuity sensor for canonical problems comprising linear and non-linear scalar conservation laws as well as the Euler equations. We show that the proposed method provides non-linear stability and captures both inter and intra-element discontinuities even for very large polynomial orders. The accuracy of the filtered solution and the effect of the filter kernel are also explored.

For the numerical results that follow, we have chosen the filter width parameter, in Eqn. (35), $\gamma = 1/3$ and the concentration sensor threshold J in Eqn. (53) to be the average of the maximum values for the cases of a centered step and a C_0 kink (see Table 1). These choices are essentially heuristic and a thorough parametric study of γ and J on the stability and accuracy of the filtered solution have been deferred to a future investigation. A preliminary study of rate of convergence as a function of γ is performed in Section 6.1.1. The unfiltered numerical solution is computed via FR using the nodal DG correction function for the spatial derivative and the standard four-stage fourth-order Runge Kutta scheme for time integration. The time step is evaluated dynamically with a value equal to half the maximum allowable time step for linear stability.

6.1. Linear advection

We begin with the case of a linear scalar conservation law obtained by substituting $f(u) = u$ in Eqn. (1) defined on $\Omega = [-1, 1]$,

$$\begin{aligned} \frac{\partial u}{\partial t} + \frac{\partial u}{\partial x} &= 0, \quad x \text{ in } [-1, 1], t > 0, \\ u(x, 0) &= u_0(x), \\ u(-1, t) &= u(1, t). \end{aligned} \quad (55)$$

In the case of a smooth initial condition, the FR solution proceeds without filtering owing to the use of the discontinuity sensor. Hence, we are interested in $u_0(x)$ of the form [11,62]

$$u_0(x) = \begin{cases} \frac{1}{6} \left(e^{-b(x+d+0.7)^2} + e^{-b(x-d+0.7)^2} + 4e^{-b(x+0.7)^2} \right), & -0.8 \leq x \leq -0.6 \\ 1, & -0.4 \leq x \leq -0.2 \\ 1 - 10|x - 0.1|, & 0.0 \leq x \leq 0.2 \\ \frac{1}{6} (F(x; 0.5 - d) + F(x; 0.5 + d) + 4F(x; 0.5)), & 0.4 \leq x \leq 0.6 \\ 0, & \text{otherwise} \end{cases} \quad (56)$$

$$F(x; z) = \sqrt{\max((1 - 100(x - z)^2), 0)},$$

with $d = 0.005$, and $b = \frac{\log(2)}{36d^2}$. This initial condition consists of a piecewise combination of Gaussian forms, a pulse, a triangle and half ellipses. Eqns. (55), (56) are solved from $t = 0$ to 8 with and without filtering for polynomial order $P = 8$ on uniform grids having $N = 6, 12, 25, 50, 100$ elements. For a comparison between kernels, the filtered solution is obtained via both Gaussian (Eqn. (34)) and box (Eqn. (37)) filters.

Figs. 2(a)–2(d) plot the results for the case of $N = 100$. In the absence of filtering, the direct numerical solution results in Gibbs phenomena at points of discontinuity. Since the flux is linear, these oscillations do not have a mechanism for causing instabilities and get advected subject to numerical dispersion. Fig. 2(b) shows the behavior of the discontinuity sensor by plotting the variation of the enhanced concentration sum in Eqn. (52) applied element-wise to the unfiltered solution. The sensor accurately picks out the location of the four jump discontinuities and almost vanishes in the smooth regions of the solution. Figs. 2(c) and 2(d) plot the solutions obtained by regular sensing and filtering operations via the Box and Gaussian filters respectively. Here, ‘regular’ implies that the operations are applied after every time-step. The action of the filter as a low-pass transfer function can be clearly observed in the filtered solution which is completely free from spurious

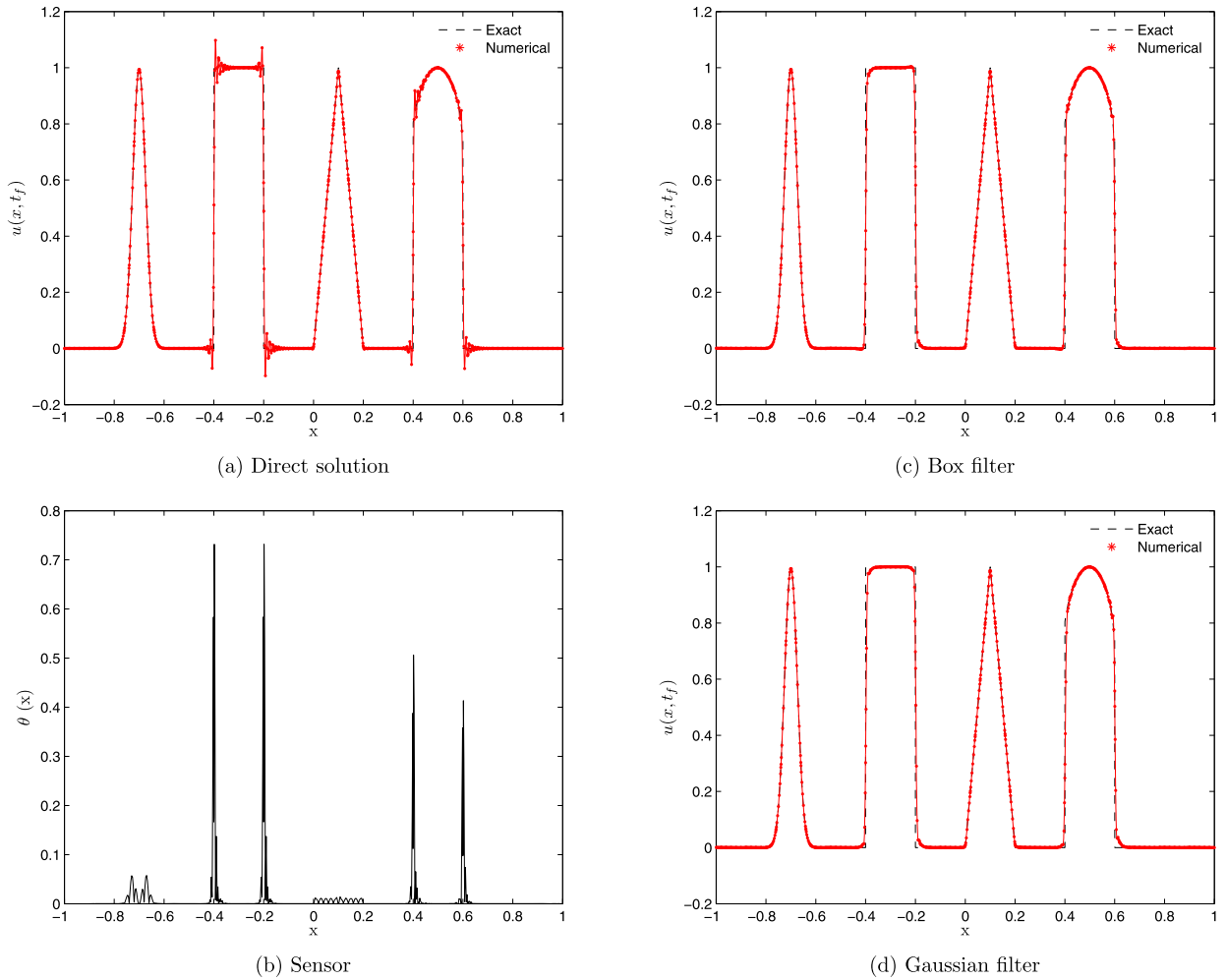


Fig. 2. Numerical solution for linear advection at $t = 8.0$ for $P = 8$, $N = 100$: (a) Direct solution via FR without filtering; (b) enhanced concentration sum, Eqn. (52), applied to the direct solution; (c) & (d) Solutions obtained with sensing and filtering operations at each time step.

Table 2
Error metrics for the numerical solution of the linear advection problem.

Case	$\ u - u^\delta\ _2$	$\ u - u^\delta\ _\infty^\delta$	$\ u - u^\delta\ _{OU}^\delta$	$TV(u^\delta) - TV(u)$
Direct solution	4.46×10^{-2}	0.4890	9.75×10^{-2}	2.60
Box-filtered	5.38×10^{-2}	0.5812	2.93×10^{-3}	5.32×10^{-2}
Gauss-filtered	6.06×10^{-2}	0.6386	6.10×10^{-12}	1.85×10^{-3}

oscillations. Additionally, owing to the sensor-selective filtering, the solution away from the discontinuities remains largely unaffected.

While the choice of filter kernel seems to have little visual effect, a quantitative comparison of the errors has been tabulated in Table 2 which includes the functional L_2 norm $\|u - u^\delta\|_2$, the discrete l_∞ norm $\|u - u^\delta\|_\infty^\delta$, the discrete maximum overshoot/undershoot $\|u - u^\delta\|_{OU}^\delta = \max(\max(u^\delta) - \max(u), \min(u) - \min(u^\delta), 0)$ and discrete total variation $TV(u^\delta) - TV(u)$. We see that the filtering reduces the overshoot/undershoot and total variation while incurring errors due to mollification of the shocks. Between the two filters, the Gaussian filter tends to have a stronger effect for the same filter width. On account of sensor-selective filtering, there does not appear to be a significant advantage of choosing one type of filter over the other.

Figs. 3(a)–3(d) show the convergence of results with grid spacing when using the box-filter. For a very coarse grid, $N = 6$, the sharp features of the solution such as the combination of Gaussians are highly dissipated on account of the inherent numerical dissipation in the discretization scheme as well as that introduced through the filter. However, with grid refinement the filtered solution recovers rapidly and appears to have little visible error at the moderate resolution of $N = 50$. In a practical setting, there may exist a region of the flow field where the numerical solution is under-resolved

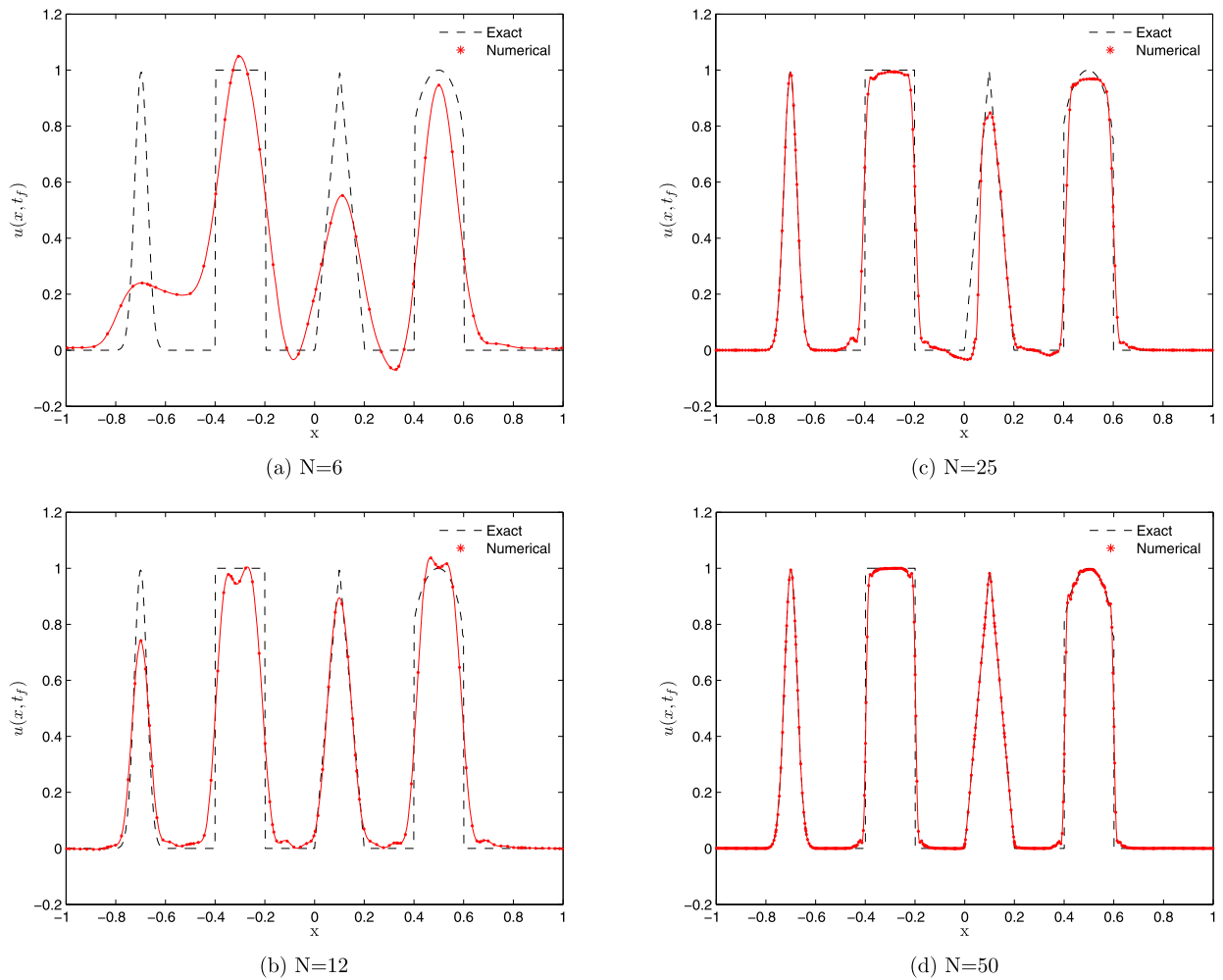


Fig. 3. Grid convergence: Box-filtered solution for linear advection at $t = 8.0$ for $P = 8$ and $N = 6, 12, 25, 50$.

and would get smoothed out by the filter due to false detection by the sensor. There are two possibilities in such a case. Either, such flow features would be a numerical artifact arising out of oscillations associated with a high-order polynomial, in which case the smoothing action would help to remove such spurious oscillations. The other possibility is when the grid is too coarse in a region where critical flow structures exist, such as a boundary layer, in which case one would need to refine the grid or change the sensor threshold J .

6.1.1. Rate of convergence for filtering without sensing

The use of a discontinuity sensor ensures that smooth regions of the solution remain unchanged. Hence, conditional on the success of the sensor, the proposed approach would preserve the order of accuracy of the underlying scheme for smooth solutions. Nevertheless, the effect of the proposed filtering operation on smooth solutions can be assessed by turning the sensor off and filtering in each element, at every time-step of the numerical solution.

Towards this end, we consider a smooth initial condition, $u_0(x) = \sin(\pi x)$, in Eqn. (55). The time-step is chosen to be 10 times smaller than the maximum allowable time step for linear stability, $\Delta t / \Delta t_{\text{CFL}} = 1/10$, so as to reduce errors associated with numerical integration. Eqn. (55) is solved from $t = 0$ to 1 with filtering in each element, at every time-step, for polynomial orders $P = 1, 2, 3, 4$ on uniform grids having $N = 8, 16$ elements. The kernel for filtering is taken to be that of the Box filter, Eqn. (37). The filter width parameter, γ , is varied over the entire range of possible values, Eqn. (38).

Fig. 4 plots the rate of convergence of the functional L_2 norm of error $\|u - u^\delta\|_2$ at $t = 1$ as a function of the filter width parameter, γ . For low values of γ , the filter transfer function is almost unity and the filtering action has negligible effect. Consequently, the filtered solution converges at the same rate as the unfiltered solution. As the filter width increases, the rate of convergence smoothly decreases to first order accuracy expected from shock capturing methods. This shows that a trade-off exists between rate of convergence and stability, i.e. as the amount of artificial dissipation introduced by the filter increases, the order of accuracy of the solution decreases. For large values of γ close to the maximum limit for positivity of

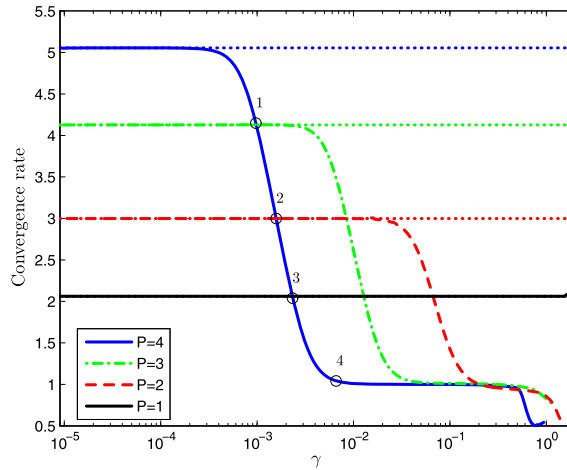


Fig. 4. Rate of convergence for linear advection with a sinusoidal initial condition, $P = 1, 2, 3, 4, N = 8, 16$ at $t = 1$: the dotted lines represent the rates for the unfiltered solution. The solid and dashed curves represent the rates as a function of the filter width parameter when the solution is filtered in each element at every time step.

Table 3

L_2 norm of error for the filtered solution at the crossover points indicated in Fig. 4 for the grid with $N = 16$ elements.

Point	$P = 1$	$P = 2$	$P = 3$	$P = 4$
1	9.57×10^{-3}	2.95×10^{-4}	6.43×10^{-6}	2.58×10^{-7}
2	9.57×10^{-3}	2.95×10^{-4}	6.44×10^{-6}	5.89×10^{-7}
3	9.57×10^{-3}	2.95×10^{-4}	6.48×10^{-6}	1.28×10^{-6}
4	9.57×10^{-3}	2.96×10^{-4}	1.02×10^{-5}	1.01×10^{-5}

the filter kernel, the filtered solution, in fact, converges sublinearly, indicating that the filtered solution is highly dissipated and of little value.

It is important to note that a decrease in order of accuracy does not imply an increase in absolute error. This can be shown by comparing the L_2 norms of error for the four P values at the crossover points marked in Fig. 4. The corresponding error values for the grid with $N = 16$ elements are tabulated in Table 3. We see that, even though the rate of convergence for $P = 4$ is decreasing with γ , the actual numerical solution is still relatively accurate. For instance, at point 4 the curve for $P = 4$ has the lowest order of accuracy but still the lowest amount of error.

6.2. Inviscid Burgers equation

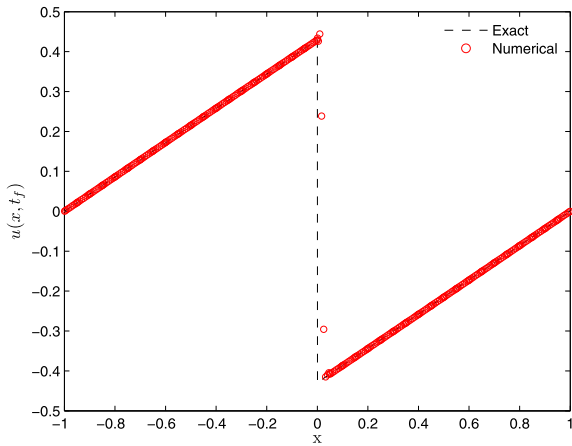
We now study the cases where the direct solution without filtering is non-linearly unstable on account of numerical instabilities. Consider the non-linear scalar conservation law obtained by substituting $f(u) = u^2$ in Eqn. (1) defined on $\Omega = [-1, 1]$,

$$\begin{aligned} \frac{\partial u}{\partial t} + \frac{\partial u^2}{\partial x} &= 0, \quad x \text{ in } [-1, 1], t > 0, \\ u(x, 0) &= -\sin(\pi x), \\ u(-1, t) &= u(1, t). \end{aligned} \tag{57}$$

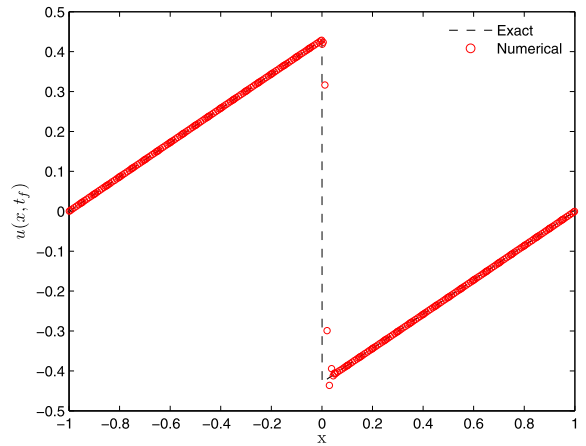
The analytical solution for Eqn. (57) can be obtained via the method of characteristics. The characteristics from the two half planes eventually coalesce into a shock located at the origin whose strength decays with time. The suitability of the filtering operation can be measured through the strength and location of the shock in the numerical solution.

Figs. 5(a) and 5(b) show the numerical solution with box-filtering and the associated point-wise error at $t = 1.0$ on a grid with $N = 40$ elements for $P = 8$. The filtered solution remains stable and accurately captures the shock strength. The error in smooth regions of the solution is at least three orders of magnitude smaller than near the shock. The filtering action spreads the shock across two solution points with the mean slightly removed from the origin. Similar results are presented in Figs. 5(c)–5(d) for $P = 7, 9$. Note that we restrict ourselves to cases with $P \geq 5$ as the performance of the chosen discontinuity sensor degrades rapidly for smaller P . An alternative sensor formulation should work seamlessly with the proposed filtering methodology.

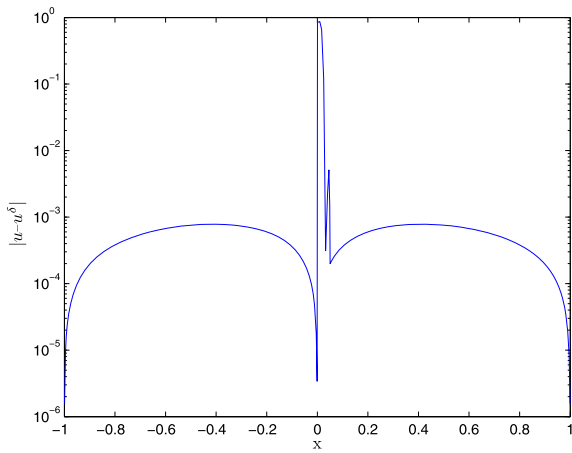
An important property of the proposed filtering approach is the ability to capture intra-element shocks. Figs. 6(a)–6(b) show the numerical solution with filtering and associated error on a grid with $N = 3$ elements for $P = 119$. We see that



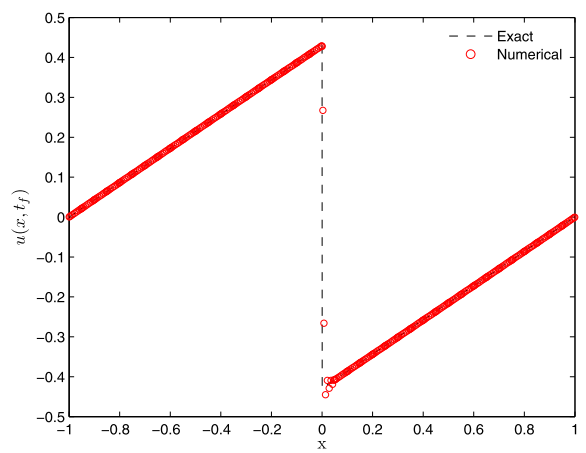
(a) Box-filtered solution, $P = 8$



(c) $P=7$

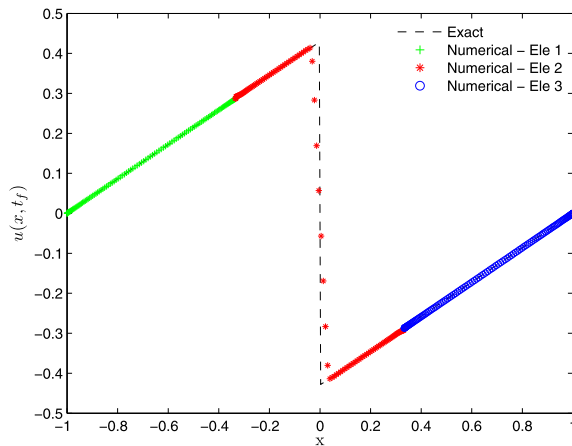


(b) Point-wise error

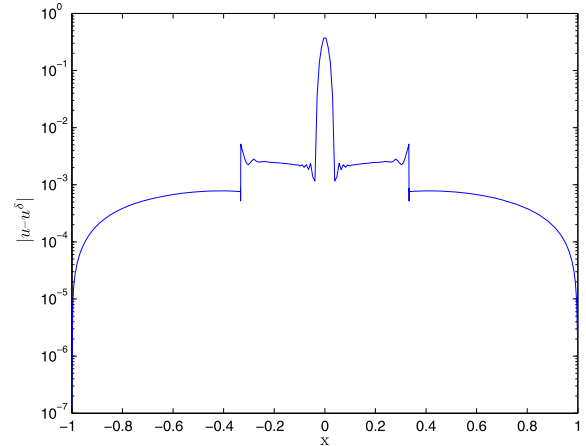


(d) $P=9$

Fig. 5. (a) Numerical solution with filtering, (b) corresponding point-wise error for Burgers equation at $t = 1.0$ for $P = 8$ and $N = 40$. (c), (d) similar results for $P = 7, 9$.



(a) Sub-element shock capturing



(b) Point-wise error

Fig. 6. (a) Numerical solution with filtering and (b) point-wise error for Burgers equation at $t = 1.0$ for $P = 119$ and $N = 3$.

both the shock location and magnitude are accurately predicted even at extremely coarse grids through such polynomial refinement. Moreover, the shock is contained completely within the interior of a single element.

6.3. Sod's shock tube

Proceeding onto a system of non-linear conservation laws, we consider the Euler equations for a calorically perfect ideal gas,

$$\frac{\partial}{\partial t} \begin{bmatrix} \rho \\ \rho u \\ \rho E \end{bmatrix} + \frac{\partial}{\partial x} \begin{bmatrix} \rho u \\ \rho u^2 + P_r \\ \rho H u \end{bmatrix} = 0, \quad \text{in } \Omega \in \mathbb{R}, t > 0,$$

$$P_r = (\gamma - 1) \left(\rho E - \frac{1}{2} \rho u^2 \right), \tag{58}$$

where ρ, u, E, P_r, H denote density, velocity, total internal energy, pressure and total enthalpy respectively, and γ denotes the ratio of specific heats. The weak form of Eqn. (58) naturally admits solutions with shocks depending on the initial and boundary conditions, and for high order polynomials, the direct numerical solution without filtering diverges due to numerical instabilities. In this subsection and the next, we show that the proposed filtering strategy leads to stable and accurate solutions. We adopt a conservative approach for dealing with a system of equations where an element is subjected to filtering if any of the conservative variables are diagnosed positively by the discontinuity sensor. Moreover, filtering is performed independently on each conservative variable directly.

Consider the initial and boundary conditions for Sod's shock tube problem [57] in $\Omega = [-1, 1]$ for $t \leq 0.57$,

$$[\rho, u, P_r]^T = \begin{cases} [1, 0, 1]^T & x < 0 \\ [0.125, 0, 0.1]^T & x \geq 0 \end{cases} \tag{59}$$

where $t \leq 0.57$ is chosen to ensure that none of the characteristics in the Riemann problem reach the boundaries of the domain. The exact solution can again be obtained using the method of characteristics and consists of a shock wave, a contact discontinuity and a smooth rarefaction fan.

Fig. 7 shows the numerical solution obtained using regular sensing and box-filtering at $t = 0.4$ on a grid with $N = 56$ elements for polynomial order $P = 8$. We see that the numerical solution accurately captures all the jumps and C_0 kinks in the solution with almost no overshoot/undershoot. The accuracy in smooth regions of the solution is preserved as well. While the location of the contact discontinuity is predicted exactly, the shock is spread over 4 points with mean slightly shifted to the right. The error metrics for each of the primitive variables are tabulated in Table 4 and confirm that stable, accurate and low total variation solutions can be obtained with high polynomial orders on coarse meshes.

6.4. Shu–Osher shock turbulence interaction

Our final test case in 1-D consists of a flow field with sinusoidal density fluctuations moving left into a stationary $Ma = 3$ normal shock front [11,35]. The domain for this case is $\Omega = [-10, 10]$ and the initial condition is prescribed as

$$[\rho, u, P_r]^T = \begin{cases} [3.857143, -0.920279, 10.333333]^T & x < 0 \\ [1 + 0.2 \sin(5x), -3.549648, 1]^T & x \geq 0 \end{cases} \tag{60}$$

The interaction leads to amplified high frequency components in the near wake and saw-tooth like skewed wave-forms in the far wake of the shock. We demonstrate that the proposed filtering approach provides stability without damping the density oscillations in the wake, and hence, can be employed for problems involving shock-vortex interactions as well.

Figs. 8(a)–(d) show the numerical solution obtained using regular sensing and box-filtering at $t = 2.0$ on successively refined grids with $N = 56, 112, 224, 448$ elements for $P = 8$. Since the analytical solution for this problem is not feasible, we use the direct solution at $t = 2.0$ for $P = 0$ on a grid with $N = 9600$ elements as the reference solution. Note that, as shown in Section 2, the case of $P = 0$ is naturally non-linearly stable and does not require any filtering. We see that the high-order numerical solution accurately captures the essential physical features of the flow including shock strength and location, amplitude and phase of the saw-tooth fluctuations in the far wake, and with grid refinement, even the high frequency components in the near wake of the shock. The solution at the finest grid suggests that the high-order scheme with careful filtering can obtain accurate results with less than half the number of degrees of freedom than the first order scheme even for solutions with strong discontinuities.

7. Numerical results in 2-D

We now validate the consistency and performance of the isotropic filtering operator formulated in Section 4.2 and Appendix A for non-linear conservation laws in two dimensions. As mentioned before, the 1-D filtering procedure can also

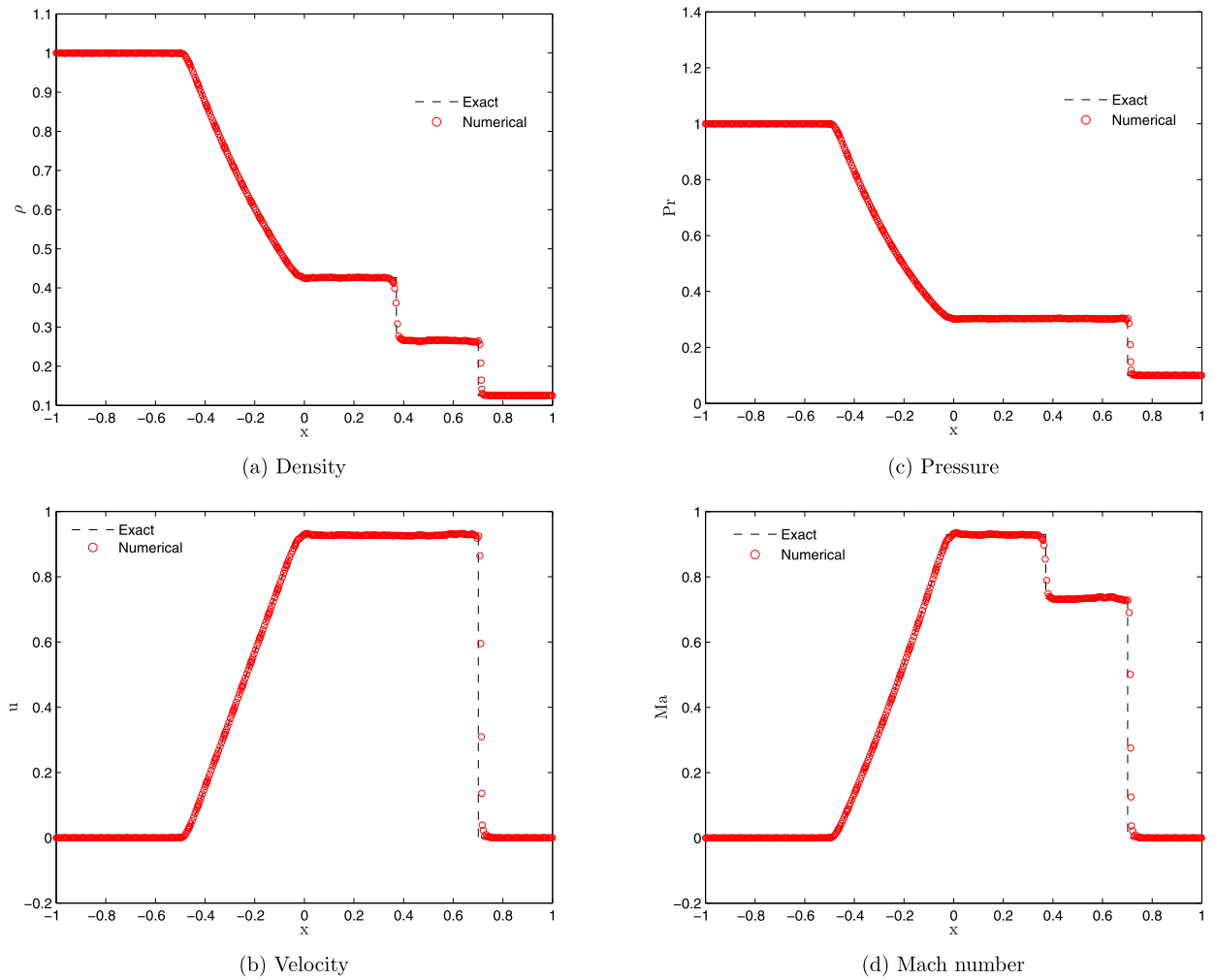


Fig. 7. Numerical solution with filtering for Sod's shock tube problem at $t = 0.4$ for $P = 8$ and $N = 56$.

Table 4

Error metrics for the numerical solution of Sod's shock tube problem. Here $Ma = u/\sqrt{\gamma P_r/\rho}$.

Case	$\ u - u^\delta\ _2$	$\ u - u^\delta\ _\infty$	$\ u - u^\delta\ _{0/U}^\delta$	$TV(u^\delta) - TV(u)$
ρ	1.51×10^{-2}	0.139652	5.29×10^{-6}	2.25×10^{-2}
u	8.98×10^{-2}	0.924835	5.38×10^{-3}	7.94×10^{-2}
P_r	1.93×10^{-2}	0.203868	5.86×10^{-6}	3.24×10^{-2}
Ma	7.26×10^{-2}	0.729450	6.41×10^{-3}	6.87×10^{-2}

be readily applied to tensor product elements by filtering along lines. A comparison of the two approaches is included in the results that follow. In order to identify elements with potential discontinuities, the concentration-based discontinuity sensor is evaluated along lines in all coordinate directions for each element.

7.1. Rigid body rotation

Consider the scalar conservation law describing counter clockwise rotation in a unit square about its center,

$$\frac{\partial u}{\partial t} + \left(\frac{1}{2} - y\right) \frac{\partial u}{\partial x} + \left(x - \frac{1}{2}\right) \frac{\partial u}{\partial y} = 0, \quad (x, y) \text{ in } [0, 1] \times [0, 1], t > 0,$$

$$u(x, y, 0) = u_0(x, y), \tag{61}$$

with periodic boundary conditions. Once again, in the case of a smooth initial condition, the FR solution proceeds without filtering owing to the use of the discontinuity sensor. Hence, we are interested in $u_0(x, y)$ of the form [12],

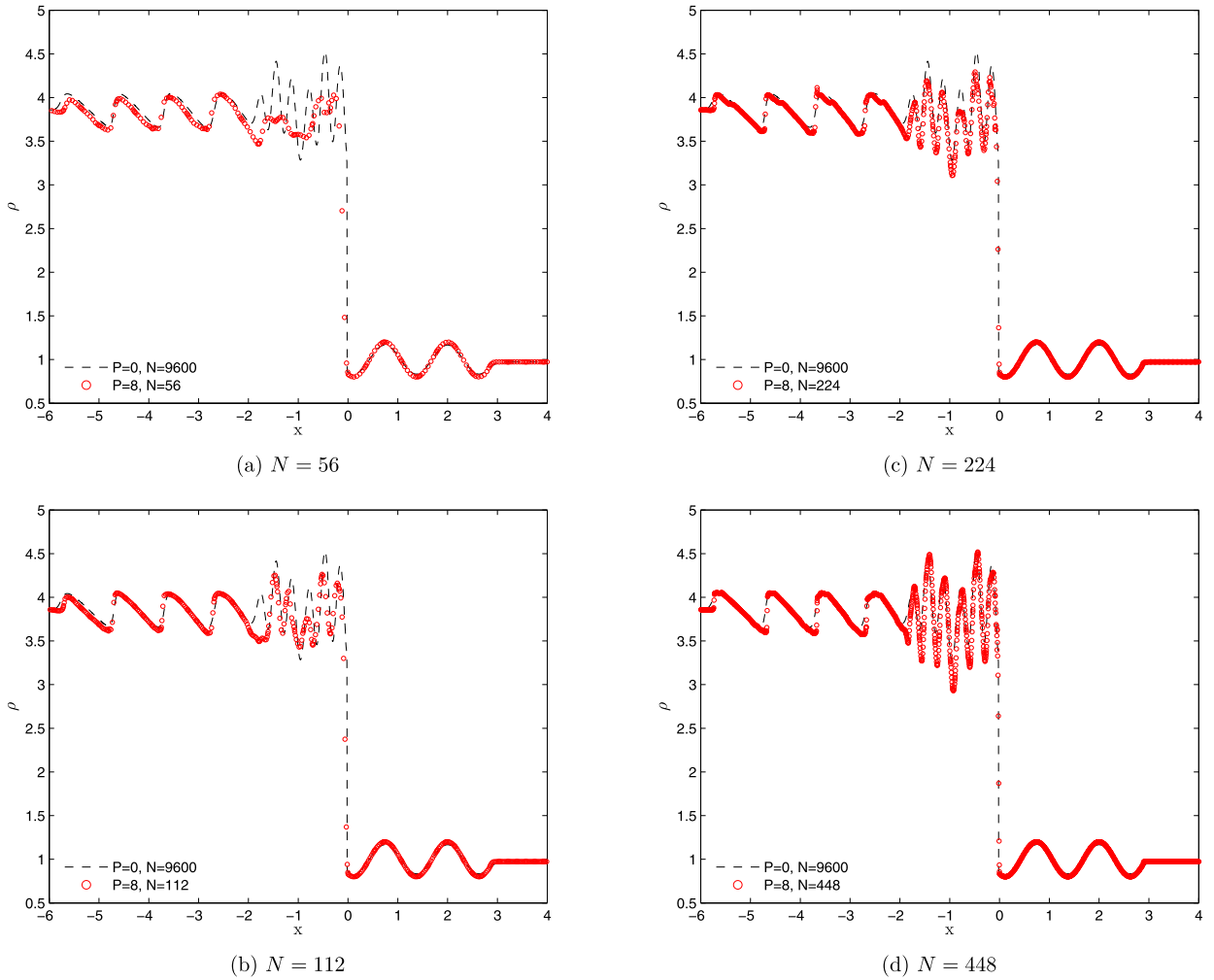


Fig. 8. Numerical solution with filtering for Shu–Osher shock turbulence interaction problem at $t = 2.0$ for $P = 8$ and $N = 56, 112, 224, 448$. The reference solution is obtained via direct solution for $P = 0, N = 9600$.

$$\begin{aligned}
 u_0(x, y) &= u_{0,1}(x, y) \mathbb{I}_{\{r(x,y;0.5,0.75) \leq 1\}} + u_{0,2}(x, y) \mathbb{I}_{\{r(x,y;0.5,0.25) \leq 1\}} \\
 &\quad + u_{0,3}(x, y) \mathbb{I}_{\{r(x,y;0.25,0.5) \leq 1\}}, \\
 r(x, y; x_0, y_0) &= \sqrt{(x - 0.5)^2 + (y - y_0)^2} / 0.15, \\
 u_{0,1}(x, y) &= \mathbb{I}_{\{|x-0.5| \geq 0.025\} \cup \{y \geq 0.85\}}, \\
 u_{0,2}(x, y) &= 1 - r(x, y; 0.5, 0.25), \\
 u_{0,3}(x, y) &= 0.25(1 + \cos(\pi r(x, y; 0.25, 0.5))),
 \end{aligned} \tag{62}$$

which consists of a slotted cylinder, a cone and a sinusoidal bump. Eqns. (61), (62) are solved for one period from $t = 0$ to 2π with and without filtering for polynomial order $P = 8$ on a uniform grid having $N = 56 \times 56$ elements. The filtered solution is evaluated using both the isotropic filter and the direct approach of filtering along lines.

We see from Fig. 9(a) that the direct numerical solution without filtering exhibits Gibbs phenomena along the circumference of the cylinder. Fig. 9(b) shows that the discontinuity sensor accurately identifies the ring of elements with jump discontinuities and almost vanishes in the smooth regions of the solution. Figs. 9(c) and 9(d) plot the solutions obtained using regular sensing and filtering operations via the isotropic Box filter and the 1-D box filter applied along lines, respectively. The filtered solution is relatively free from spurious oscillations and, owing to sensor-selective filtering, the solution away from the discontinuities remains largely unaffected. A quantitative comparison of the errors has been tabulated in Table 5 which includes the discrete l_2 norm $\|u - u^\delta\|_2^\delta$, the discrete l_∞ norm $\|u - u^\delta\|_\infty^\delta$ and the discrete maximum overshoot/undershoot $\|u - u^\delta\|_{0/U}^\delta$. We see that both the filtering strategies reduce error along all metrics with relatively little difference between them.

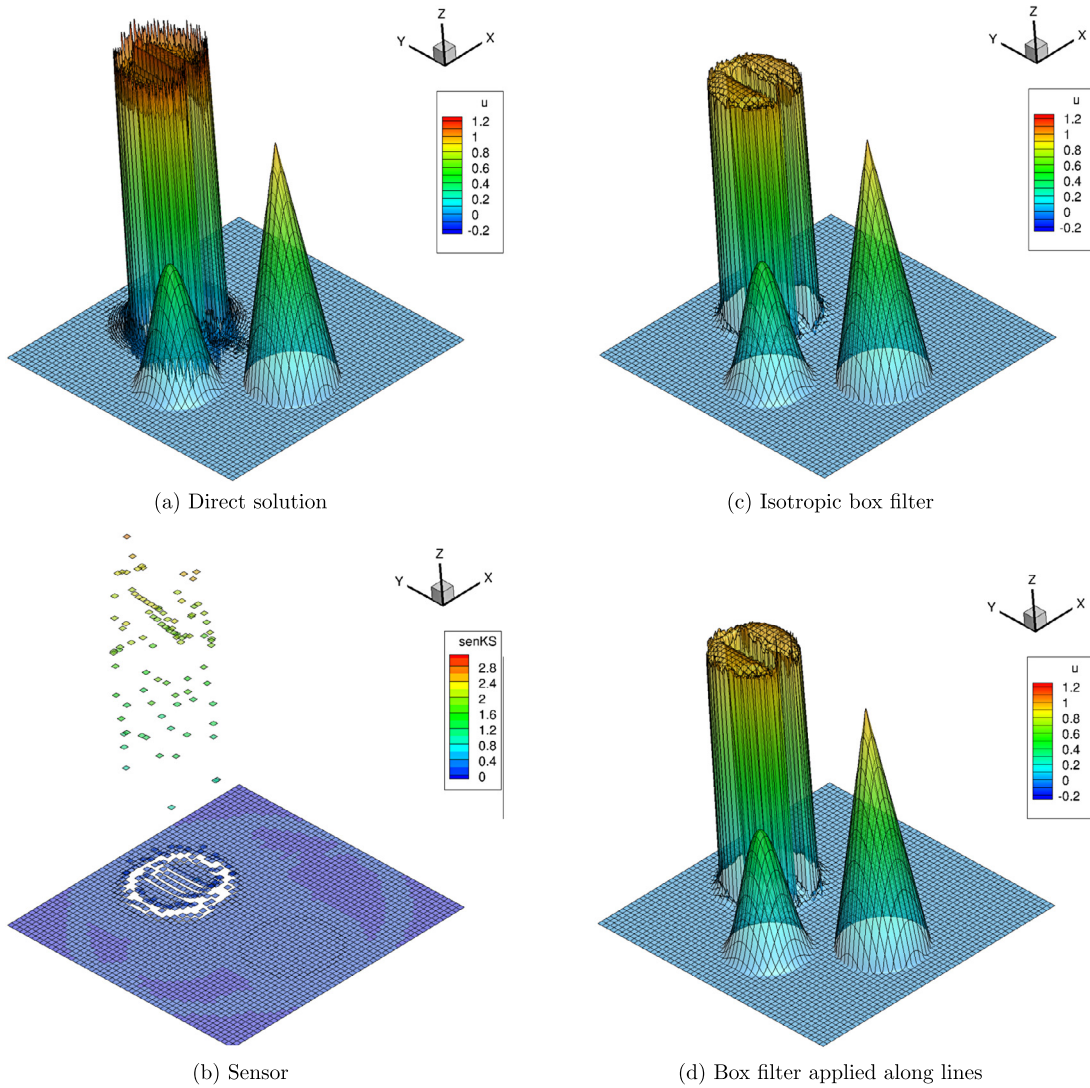


Fig. 9. Numerical solution for rigid body rotation at $t = 2\pi$ for $P = 8$, $N = 56 \times 56$: (a) Direct solution via FR without filtering; (b) enhanced concentration sum, Eqn. (52), applied to the direct solution along lines; (c) & (d) Solutions obtained with sensing and filtering operations at each time step.

Table 5
Error metrics for the numerical solution of the rigid body rotation problem.

Case	$\ u - u^\delta\ _2^\delta$	$\ u - u^\delta\ _\infty^\delta$	$\ u - u^\delta\ _{0/U}^\delta$
Direct solution	5.95×10^{-3}	6.40×10^{-4}	6.40×10^{-4}
Isotropic box filter	1.30×10^{-4}	2.06×10^{-5}	2.06×10^{-5}
1-D box filter along lines	1.20×10^{-4}	1.57×10^{-5}	1.57×10^{-5}

7.2. Symmetric Riemann problem

Proceeding onto a system of non-linear conservation laws, we now consider the 2-D extension of the Euler equations, Eqns. (58), for a calorically perfect ideal gas,

$$\frac{\partial}{\partial t} \begin{bmatrix} \rho \\ \rho u \\ \rho v \\ \rho E \end{bmatrix} + \frac{\partial}{\partial x} \begin{bmatrix} \rho u \\ \rho u^2 + P_r \\ \rho uv \\ \rho Hu \end{bmatrix} + \frac{\partial}{\partial y} \begin{bmatrix} \rho v \\ \rho uv \\ \rho v^2 + P_r \\ \rho Hv \end{bmatrix} = 0, \quad \text{in } \Omega \in \mathbb{R}, t > 0,$$

$$P_r = (\gamma - 1) \left(\rho E - \frac{1}{2} \rho (u^2 + v^2) \right), \tag{63}$$

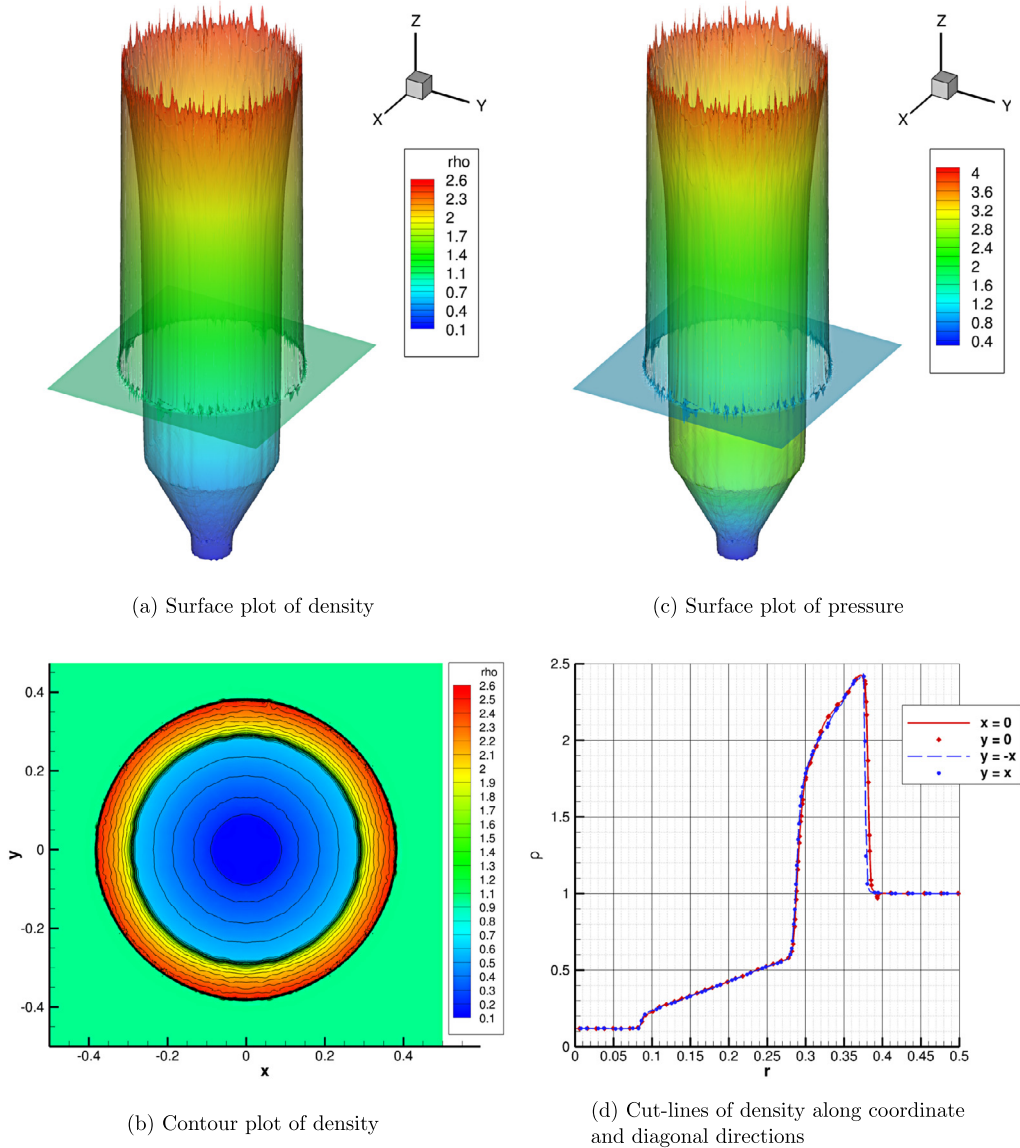


Fig. 10. Numerical solution with isotropic box filtering for radially symmetric Riemann problem at $t = 0.1$ for $P = 8$ and $N = 56 \times 56$.

where u and v now denote the x and y velocities respectively. As in 1-D, the weak form of Eqn. (63) admits solutions with shocks depending on the initial and boundary conditions. For high-order polynomials, the direct numerical solution without filtering diverges due to numerical instabilities. Consider the radially symmetric Riemann problem [12] in $\Omega = [-\frac{1}{2}, \frac{1}{2}] \times [-\frac{1}{2}, \frac{1}{2}]$,

$$[\rho, u, v, P_r]^T = \begin{cases} [2, 0, 0, 15]^T & \sqrt{x^2 + y^2} < 0.13 \\ [1, 0, 0, 1]^T & \sqrt{x^2 + y^2} \geq 0.13 \end{cases} \tag{64}$$

which consists of a shock wavefront expanding radially outwards, a contact discontinuity and, most importantly, a rarefaction fan that moves radially inwards towards the origin creating a depression with a carbuncle. Thus, unlike the 1-D shock tube, the solution is not L_∞ preserving and highlights the importance of appropriate normalization of the solution for sensing discontinuities.

Fig. 10 shows the numerical solution obtained using regular sensing and box-filtering at $t = 0.1$ on a grid with $N = 56 \times 56$ elements for polynomial order $P = 8$. We see that the numerical solution accurately captures all the jumps and C_0 discontinuities in the solution including the low density depression and carbuncle in the interior of the domain. Additionally, cutlines of density in the coordinate and diagonal directions show that the numerical solution preserves radial symmetry.

7.3. Double Mach reflection

Our final test case for this paper is the double Mach reflection problem of Woodward and Colella [58], in $\Omega = [0, 4] \times [0, 1]$, wherein a Mach 10 shock is incident on a reflecting wall at an angle of 60° . A detailed description of the physical problem, self-similarity of the solution and the boundary conditions can be found in [58]. The complexity of treating oblique walls is avoided by tilting the domain so that the reflecting wall is aligned with the x -axis. The reflected shock is kept attached to the reflecting wall by assigning post-shock values for $\{x \in [0, 1/6], y = 0\}$. A time varying boundary condition is applied on the top wall, $y = 1$, to describe the exact motion of the shock. Details regarding the implementation of the initial and boundary conditions can be found in [12].

Fig. 11 shows the numerical solution obtained using regular sensing and box-filtering at $t = 0.2$ on a grid with $N = 56 \times 224$ elements for polynomial order $P = 8$. For this case of severely high shock strength, the threshold for the discontinuity sensor, J , was reduced to the corresponding value for a C_0 kink (see Table 1) in order to compute stably.

We see that, even at this coarse grid, the filtered solution consistently predicts the two Mach shocks, the contact discontinuities and the jet of dense fluid issued to the right from the base of the first contact discontinuity. However, in the region bounded by the curved reflected shock and the wall, contours of physical variables are visibly marked with high frequency noise. As predicted by Woodward and Colella, such oscillations occur since the dissipation added through the Riemann fluxes at element interfaces vanishes in the limit of zero flow velocity. Note that artificial dissipation is not added through the filter in this region since the fluctuations are too small to trigger a positive response from the discontinuity sensor. Finally, we can see that the solution also exhibits the ‘starting error’ associated with the spreading of the shock during the collocation projection of the initial condition. This is manifested most clearly in the strip originating from the upper right corner of the contour plot for v_y . Note that the flood plot reveals that this spurious contour separates levels that differ only slightly in magnitude.

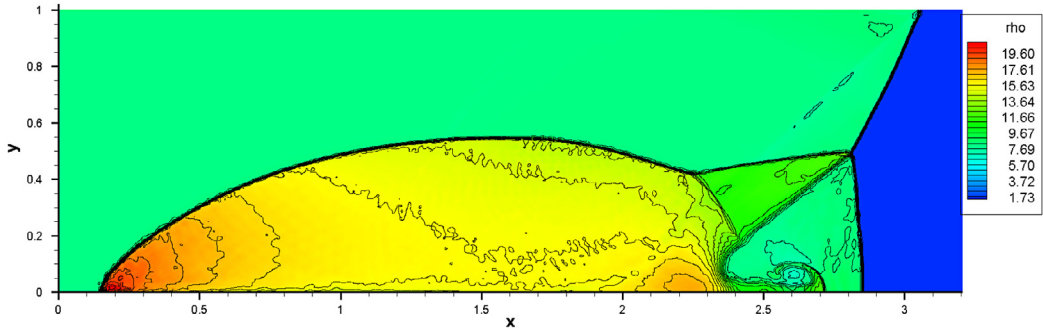
8. Conclusions

The contributions of this study can be divided into two segments. The first one is concerned with theoretical developments regarding non-linear stability of high-order Flux Reconstruction (FR) schemes. Energy bounds on the numerical solution via FR have been obtained to show that aliasing errors may not vanish even in the asymptotic limit on polynomial order, $P \rightarrow \infty$, if the analytical flux function is not sufficiently smooth. However, the addition of adequate artificial dissipation can ensure non-linear stability. Convergence in the asymptotic limit is proven in Theorem 3.1 which provides the rate of growth of dissipation coefficients with h and P . Stability for any given polynomial order is guaranteed by Theorem 3.2 for all grids finer than a critical grid resolution. An unstable numerical solution can be stabilized by either increasing the strength of dissipation or decreasing the grid spacing.

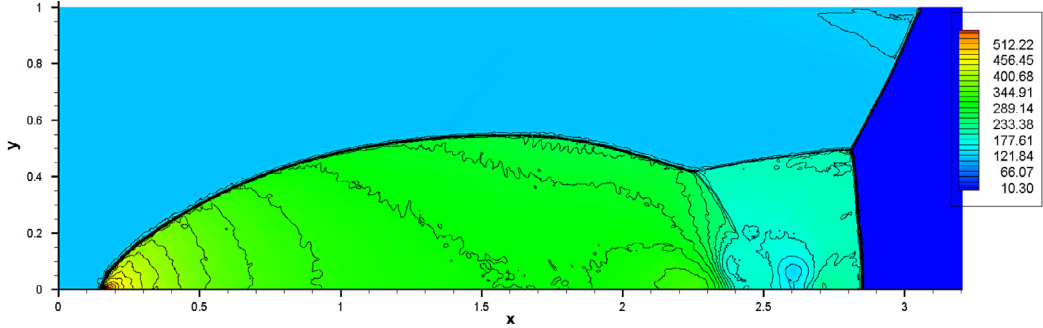
The second segment is concerned with the design of a computationally efficient and consistent mechanism for introducing artificial dissipation that conforms to the derived conditions. For this purpose, artificial viscosity is posed as a Fourier filtering operation which is then implemented in the physical space via convolution. This avoids the costly computation of several derivatives while preserving the dispersion properties of the actual FR formulation. The convolution integral is approximated by a strictly local stencil by padding the solution in a given element with the edge information from neighboring elements. This step plays a critical role in controlling inter-element discontinuities. The filter is selectively applied to troubled cells as indicated by a discontinuity sensor based on the spectral concentration method of Tadmor et al. This ensures that the smooth regions of the solution remain unchanged and local accuracy is maintained away from the shocks.

Numerous numerical tests in 1-D and 2-D have been performed to validate the theoretical results. The proposed sensing and filtering approach allows stable computations of non-linear conservation laws by capturing shock discontinuities while preserving accuracy in smooth regions of the solution. The shock strength is predicted accurately even for very high polynomial orders such as $P = 119$. Moreover, it is possible to capture intra-element shocks wherein the shock is completely localized in the interior of an element. Tougher problems involving interaction of severely strong shocks with fine flow structures are also amenable to high-order schemes such as $P = 8$ with appropriate filtering. Perhaps, the only limitation is in regard to the slight mis-prediction of shock speeds for slow moving shocks, probably owing to the use of approximate Riemann solvers for calculating common interface fluxes in FR. Finally, even for linear conservation laws, the filtered solution provides significantly reduced total variation, maximum overshoot/undershoot and discrete error norms. The effect of filtering on smooth solutions has been studied by turning the sensor off and filtering in each element at every time-step. The rate of convergence for such cases varies smoothly as a function of the filter width, starting at the convergence rate of the unfiltered solution and dropping down to first order for large widths. This re-emphasizes the need for a reliable discontinuity sensor.

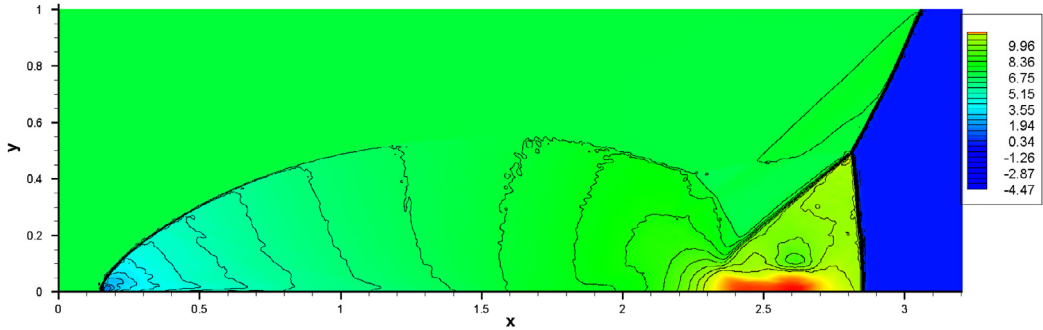
Note that the theoretical results in this study are limited to scalar conservation laws in 1-D. While an extension to vector conservation laws for tensor-product elements in higher dimensions has been proposed, a rigorous proof of stability is still lacking. Hence, this preliminary study can be regarded as the first investigation into non-linear stability theory for the FR formulation. We have shown that numerical solutions of arbitrary polynomial order can be stabilized with adequate artificial dissipation under exact time integration. The primary task ahead is to generalize the stability theory to the Euler and Navier–Stokes equations and to explore the effects of numerical time integration on the stability properties. Subsequently, it is important to extend the filter formulation to simplex elements. This can be achieved by considering the modal analogue



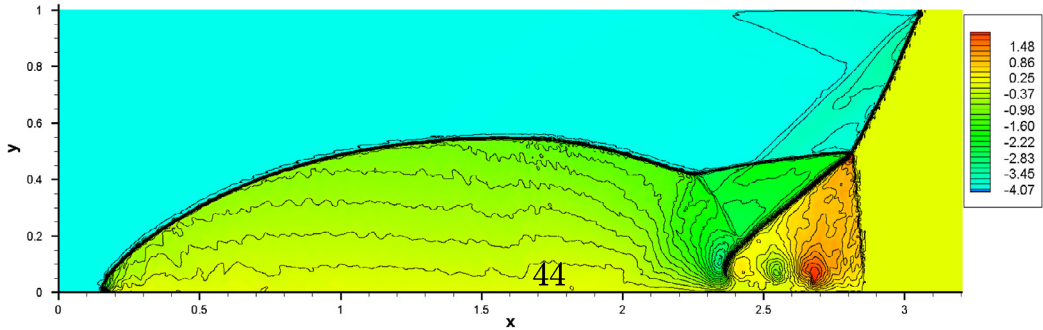
(a) Density: 30 isolines: 1.731 to 20.92



(b) Pressure: 30 isolines: 10.30 to 549.4



(c) x-velocity: 30 isolines: -4.47 to 11.28



(d) y-velocity: 30 isolines: -4.065 to 1.891

Fig. 11. Numerical solution with isotropic box filtering for double Mach reflection problem at $t = 0.1$ for $P = 8$ and $N = 56 \times 224$.

of the general framework proposed for quadrilaterals. Additionally, the proposed approach would benefit from a better discontinuity sensor that works for moderate and low values of polynomial orders as well. Finally, a parametric study of the sensor threshold, J , and the filter parameter, γ , is needed to enable adaptivity in the sensing and filtering operations.

Acknowledgements

This work was supported by Air Force Office of Scientific Research, AFOSR, Grant # FA9550-14-1-0186 monitored by Dr. Fariba Fahroo. The first author would like to acknowledge support from the Thomas V Jones Stanford Graduate Fellowship. The authors are grateful to David Williams³ for his detailed comments regarding the manuscript and insightful suggestions concerning the proof in Section 3.

Appendix A. Local filter formulation in 2-D for tensor product elements

As before, we begin by defining an operator \mathcal{P}^2 that pads the piecewise polynomial solution in the parent space $\hat{u}^\delta(r_1, r_2)$ with the edge values of the neighboring elements,

$$\begin{aligned} \hat{v}_n(r_1, r_2) &= \mathcal{P}^2(\hat{u}^\delta(r_1, r_2)) \\ &= \hat{u}_n^\delta(r_1, r_2)\mathbb{I}_{(-1,1)\times(-1,1)}(r_1, r_2) \\ &\quad + \hat{u}_{nL}^\delta(1, r_2)\mathbb{I}_{(-\infty, -1]\times(-1,1)} + \hat{u}_{nR}^\delta(-1, r_2)\mathbb{I}_{[1,\infty)\times(-1,1)} \\ &\quad + \hat{u}_{nD}^\delta(r_1, 1)\mathbb{I}_{(-1,1)\times(-\infty, -1]} + \hat{u}_{nU}^\delta(r_1, -1)\mathbb{I}_{(-1,1)\times[1,\infty)} \\ &\quad + \hat{u}_{nLD}^\delta(1, 1)\mathbb{I}_{(-\infty, -1]\times(-\infty, -1]} + \hat{u}_{nDR}^\delta(-1, 1)\mathbb{I}_{[1,\infty)\times(-\infty, -1]} \\ &\quad + \hat{u}_{nUR}^\delta(-1, -1)\mathbb{I}_{[1,\infty)\times[1,\infty)} + \hat{u}_{nLU}^\delta(1, -1)\mathbb{I}_{(-\infty, -1]\times[1,\infty)}, \end{aligned} \quad (\text{A.1})$$

where $L, R, U, D, LD, DR, UR, LU$ denote the neighboring elements as illustrated in Fig. 1(b). The convolution integral can now be simplified as

$$\begin{aligned} \bar{v}_n(r_1, r_2) &= \int_{-\infty}^{\infty} \int_{-\infty}^{\infty} \hat{v}_n(s_1, s_2) \hat{g}_{2D}(x_1(r_1) - x_1(s_1), x_2(r_2) - x_2(s_2); \Delta) J_n ds_1 ds_2 \\ &= \int_{-\infty}^{\infty} \int_{-\infty}^{\infty} \hat{v}_n(s_1, s_2) \hat{g}(x_1(r_1) - x_1(s_1); \Delta J_n^{-1/2}) \hat{g}(x_2(r_2) - x_2(s_2); \Delta J_n^{-1/2}) ds_1 ds_2. \end{aligned} \quad (\text{A.2})$$

We now partition this double integral into the nine pieces depicted in Fig. 1(b) and substitute \hat{v}_n from Eqn. (A.1). While the expressions can be directly evaluated using numerical integration, it would result in separate matrices for each element on account of the non-uniform Jacobian terms. In the case of quadrilaterals with parallel edges, the Jacobian is constant and the operation gets significantly simplified:

$$\begin{aligned} \bar{v}_n(r_1, r_2) &= \sum_{p_1=1, p_2=1}^{P+1, P+1} \hat{u}_{n, p_1, p_2}^\delta w_{p_1}(r_1) w_{p_2}(r_2) \\ &\quad + \hat{u}_{nL}^\delta(1, r_2) w_0(r_1) w_{p_2}(r_2) + \hat{u}_{nR}^\delta(-1, r_2) w_{P+2}(r_1) w_{p_2}(r_2) \\ &\quad + \hat{u}_{nD}^\delta(r_1, 1) w_{p_1}(r_1) w_{P+2}(r_2) + \hat{u}_{nU}^\delta(r_1, -1) w_{p_1}(r_1) w_0(r_2) \\ &\quad + \hat{u}_{nLD}^\delta(1, 1) w_0(r_1) w_0(r_2) + \hat{u}_{nDR}^\delta(-1, 1) w_{P+1}(r_1) w_0(r_2) \\ &\quad + \hat{u}_{nUR}^\delta(-1, -1) w_{P+2}(r_1) w_{P+2}(r_2) + \hat{u}_{nLU}^\delta(1, -1) w_0(r_1) w_{P+2}(r_2), \end{aligned} \quad (\text{A.3})$$

where $\hat{\Delta} = \Delta J_n^{-1/2}$ is the constant filter width in the parent domain. Once again, this linear scaling results in a constant filter width in the parent space. This procedure can again be conveniently expressed as a matrix-vector product

$$\bar{u}_{p_1, p_2} = w_i(r_{p_1}) w_j(r_{p_2}) \hat{v}_{i, j}, \quad \text{for } 1 \leq p_1, p_2 \leq P+1, \quad (\text{A.4})$$

where the contraction is performed over $0 \leq i, j \leq P+2$, and the vector of padded solution values is given by

³ CFD Engineer, Flight Sciences division, Boeing Commercial Airplanes.

$$\hat{v}_{i,j} = \begin{cases} u_{n,i,j}^\delta & 1 \leq i, j \leq P+1 \\ u_{nL}^\delta(1, r_2) & i=0, 1 \leq j \leq P+1 \\ u_{nR}^\delta(-1, r_2) & i=P+2, 1 \leq j \leq P+1 \\ u_{nD}^\delta(r_1, 1) & 1 \leq i \leq P+1, j=0 \\ u_{nU}^\delta(r_1, -1) & 1 \leq i \leq P+1, j=P+2 \\ u_{nLD}^\delta(1, 1) & i=0, j=0 \\ u_{nDR}^\delta(-1, 1) & i=P+2, j=0 \\ u_{nUR}^\delta(-1, -1) & i=P+2, j=P+2 \\ u_{nLU}^\delta(1, -1) & i=0, j=P+2 \end{cases} \quad (\text{A.5})$$

The resultant filtering matrix \mathbf{F} is of dimensions $(P+1)^2 \times (P+3)^2$.

References

- [1] G. Chavent, B. Cockburn, The local projection P^0P^1 -discontinuous-Galerkin finite element method for scalar conservation laws, *RAIRO, Model. Math. Anal. Numer.* 23 (1989) 565.
- [2] P. Lesaint, P.A. Raviart, On a finite element method for solving the neutron transport equation, in: *Mathematical Aspects of Finite Elements in Partial Differential Equations*, Academic Press, San Diego, 1974, p. 89.
- [3] W.H. Reed, T.R. Hill, Triangular mesh methods for the neutron transport equation, Los Alamos Scientific Laboratory Report LA-UR-73-479, 1973.
- [4] J.S. Hesthaven, T. Warburton, *Nodal Discontinuous Galerkin Methods*, Springer Texts in Applied Mathematics, vol. 54, 2008.
- [5] R. Hartmann, P. Houston, Adaptive discontinuous Galerkin finite element methods for the compressible Euler equations, *J. Comput. Phys.* 183 (2002) 508–532.
- [6] J. Remacle, J.E. Flaherty, M.S. Shephard, An adaptive discontinuous Galerkin technique with an orthogonal basis applied to compressible flow problems, *SIAM Rev.* 45 (1) (2003) 53–72.
- [7] J.J.W. van der Vegt, H. van der Ven, Discontinuous Galerkin finite element method with anisotropic local grid refinement for inviscid compressible flows, *J. Comput. Phys.* 141 (1998) 46–77.
- [8] K.J. Fidkowski, D.L. Darmofal, Review of output-based error estimation and mesh adaptation in computational fluid dynamics, *AIAA J.* 49 (2011) 673–694.
- [9] B. van Leer, Towards the ultimate conservative difference scheme. V. A second-order sequel to Godunov's method, *J. Comput. Phys.* 32 (1979) 101–136.
- [10] R. Biswas, K.D. Devine, J.E. Flaherty, Parallel, adaptive finite element methods for conservation laws, *Appl. Numer. Math.* 14 (1994) 255–283.
- [11] L. Krivodonova, Limiters for high-order discontinuous Galerkin methods, *J. Comput. Phys.* 226 (2007) 879–896.
- [12] D. Kuzmin, Hierarchical slope limiting in explicit and implicit discontinuous Galerkin methods, *J. Comput. Phys.* 257 (2014) 1140–1162.
- [13] A. Burbeau, P. Sagaut, Ch.-H. Bruneau, A problem-independent limiter for high-order Runge–Kutta discontinuous Galerkin methods, *J. Comput. Phys.* 169 (2001) 111–150.
- [14] M.R. Visbal, D.V. Gaitonde, Very high-order spatially implicit schemes for computational acoustics on curvilinear meshes, *J. Comput. Acoust.* 09 (2001) 1259.
- [15] T.K. Sengupta, Y. Bhumkar, V. Lakshmanan, Design and analysis of a new filter for LES and DES, *Comput. Struct.* 87 (2009) 735–750.
- [16] O.V. Vasilyev, T.S. Lund, P. Moin, A general class of commutative filters for LES in complex geometries, *J. Comput. Phys.* 146 (1998) 82–104.
- [17] H.M. Blackburn, S. Schmidt, Spectral element filtering techniques for large eddy simulation with dynamic estimation, *J. Comput. Phys.* 186 (2003) 610–629.
- [18] P. Sagaut, R. Grohen, Discrete filters for large eddy simulation, *Int. J. Numer. Methods Fluids* 31 (1999) 1195–1220.
- [19] N.A. Adams, S. Stolz, A subgrid-scale deconvolution approach for shock capturing, *J. Comput. Phys.* 178 (2002) 391–426.
- [20] C. Bogey, N. Cacquaray, C. Bailly, A shock-capturing methodology based on adaptive spatial filtering for high-order non-linear computations, *J. Comput. Phys.* 228 (2009) 1447–1465.
- [21] H. van der Ven, A family of large eddy simulation (LES) filters with nonuniform filter widths, *Phys. Fluids* 7 (1995) 1171.
- [22] E. Tadmor, Super viscosity and spectral approximations of nonlinear conservation laws, in: *Numerical Methods for Fluid Dynamics. IV*, February 14, 1999, pp. 69–82.
- [23] J.S. Hesthaven, S. Gottlieb, D. Gottlieb, *Spectral Methods for Time-Dependent Problems*, Cambridge Monographs on Applied and Computational Mathematics, vol. 21, Cambridge University Press, 2007.
- [24] J.S. Hesthaven, R.M. Kirby, Filtering in Legendre spectral methods, *Math. Comput.* 77 (263) (2008) 1425–1452.
- [25] A. Meister, S. Ortleb, Th. Sonar, Application of spectral filtering to discontinuous Galerkin methods on triangulations, *Numer. Methods Partial Differ. Equ.* (2011), <http://dx.doi.org/10.1002/num.20705>.
- [26] H. Vandeven, Family of spectral filters for discontinuous problems, *J. Sci. Comput.* 6 (2) (1991).
- [27] D. Gottlieb, C.-W. Shu, On the Gibbs phenomenon and its resolution, *SIAM Rev.* 39 (4) (1997) 644–668.
- [28] D. Gottlieb, J.S. Hesthaven, Spectral methods for hyperbolic problems, *J. Comput. Appl. Math.* 128 (2001) 83–131.
- [29] H. Mirzaee, J.K. Ryan, R.M. Kirby, Smoothness-increasing accuracy-conserving (SIAC) filters for discontinuous Galerkin solutions: application to structured tetrahedral meshes, *J. Sci. Comput.* (2013), <http://dx.doi.org/10.1007/s10915-013-9748-2>.
- [30] J. Zhu, X. Zhong, C.-W. Shu, J. Qiu, Runge–Kutta discontinuous Galerkin method using a new type of WENO limiters on unstructured meshes, *J. Comput. Phys.* 248 (2013) 200–220.
- [31] L. Krivodonova, J. Xin, J.-F. Remacle, N. Chevaugeon, J.E. Flaherty, Shock detection and limiting with discontinuous Galerkin methods for hyperbolic conservation laws, *Appl. Numer. Math.* 48 (2004) 323–338.
- [32] P. Persson, J. Peraire, Sub-cell shock capturing for discontinuous Galerkin methods, in: *44th AIAA Aerospace Sciences Meeting and Exhibit 9–12 January 2006*, Reno, Nevada.
- [33] G.E. Barter, D.L. Darmofal, Shock capturing with higher-order, PDE-based artificial viscosity, in: *18th AIAA Computational Fluid Dynamics Conference 25–28 June 2007*, Miami, FL.
- [34] W. Cai, D. Gottlieb, C.-W. Shu, Essentially nonoscillatory spectral Fourier methods for shock wave calculations, *Math. Comput.* 52 (186) (1989) 389–410.
- [35] C.-W. Shu, S. Oshers, Efficient implementation of essentially non-oscillatory shock-capturing schemes. II, *J. Comput. Phys.* 83 (1989) 32–78.
- [36] A.W. Cook, W.H. Cabot, Hyperviscosity for shock–turbulence interaction, *J. Comput. Phys.* 203 (2005) 379–385.

- [37] S. Kawai, S.K. Lele, Localized artificial diffusivity scheme for discontinuity capturing on curvilinear meshes, *J. Comput. Phys.* 227 (2008) 9498–9526.
- [38] E. Tadmor, The numerical viscosity of entropy stable schemes for systems of conservation laws. I, *Math. Comput.* 49 (1987) 91–103.
- [39] E. Tadmor, Entropy stability theory for difference approximations of nonlinear conservation laws and related time dependent problems, *Acta Numer.* 12 (2003) 451–512.
- [40] M. Svård, S. Mishra, Shock capturing artificial dissipation for high-order finite difference schemes, *J. Sci. Comput.* 39 (2009) 454–484.
- [41] T.C. Fisher, M.H. Carpenter, High-order entropy stable finite difference schemes for nonlinear conservation laws: finite domains, *J. Comput. Phys.* 252 (2013) 518–557.
- [42] M.H. Carpenter, T.C. Fisher, E.J. Nielsen, S.H. Frankel, Entropy stable spectral collocation schemes for the Navier–Stokes equations: discontinuous interfaces, *SIAM J. Sci. Comput.* 36 (2014) B835–B867.
- [43] H.T. Huynh, A flux reconstruction approach to high-order schemes including discontinuous Galerkin methods, *AIAA Conference Paper 2007–4079*.
- [44] P. Castonguay, P.E. Vincent, A. Jameson, A new class of high-order energy stable flux reconstruction schemes for triangular elements, *J. Sci. Comput.* 51 (1) (2012) 224–256.
- [45] D.M. Williams, A. Jameson, Energy stable flux reconstruction schemes for advection–diffusion problems on tetrahedra, *J. Sci. Comput.* (2013).
- [46] D.A. Kopriva, J.H. Kalias, A conservative staggered-grid Chebyshev multidomain method for compressible flows, *J. Comput. Phys.* 125 (1996) 244–261.
- [47] Y. Liu, M. Vinokur, Z.J. Wang, Spectral difference method for unstructured grids I: basic formulation, *J. Comput. Phys.* 216 (2006) 780–801.
- [48] K. Asthana, A. Jameson, High-order flux reconstruction schemes with minimal dispersion and dissipation, *J. Sci. Comput.* (2014), <http://dx.doi.org/10.1007/s10915-014-9882-5>.
- [49] M. Lopez, K. Asthana, A. Jameson, Families of provably-stable flux reconstruction schemes with correction functions continuous in m derivatives, *Comput. Methods Appl. Mech. Eng.* (2015), submitted for publication.
- [50] P.E. Vincent, P. Castonguay, A. Jameson, A new class of high-order energy stable flux reconstruction schemes, *J. Sci. Comput.* 47 (1) (2011) 50–72.
- [51] P.E. Vincent, P. Castonguay, A. Jameson, Insights from von Neumann analysis of high-order flux reconstruction schemes, *J. Comput. Phys.* 230 (2011) 8134–8154.
- [52] A. Jameson, P.E. Vincent, P. Castonguay, On the non-linear stability of flux reconstruction schemes, *J. Sci. Comput.* 50 (2) (2012) 434–445.
- [53] A. Gelb, E. Tadmor, Detection of edges in spectral data, *Appl. Comput. Harmon. Anal.* 7 (1999) 101–135.
- [54] A. Gelb, E. Tadmor, Detection of edges in spectral data. II-Nonlinear enhancement, *SIAM J. Numer. Anal.* 38 (4) (2000) 1389–1408.
- [55] Anne Gelb, Dennis Cates, Detection of edges in spectral data III-refinement of the concentration method, *J. Sci. Comput.* 36 (2008) 1–43.
- [56] A. Sheshadri, A. Jameson, Shock detection and capturing methods for high order discontinuous-Galerkin finite element methods, in: *32nd AIAA Applied Aerodynamics Conference*, Atlanta, GA, 16–20 June 2014, *AIAA 2014-2688*.
- [57] G.A. Sod, A survey of several finite difference methods for systems of nonlinear hyperbolic conservation laws, *J. Comput. Phys.* 27 (1978).
- [58] P. Woodward, P. Colella, The numerical simulation of two-dimensional fluid flow with strong shocks, *J. Comput. Phys.* 54 (1) (April 1984) 115–173.
- [59] C. Canuto, A. Quarteroni, Approximation results for orthogonal polynomials in Sobolev spaces, *Math. Comput.* 38 (157) (January 1982).
- [60] C. Bernardi, Yvon Maday, Polynomial interpolation results in Sobolev spaces, *J. Comput. Appl. Math.* 43 (1992) 53–80.
- [61] J.R. Bull, A. Jameson, Simulation of the compressible Taylor Green vortex using high-order flux reconstruction schemes, in: *7th AIAA Theoretical Fluid Mechanics Conference*, 16–20 June 2014, Atlanta, GA, *AIAA Paper 2014-3210*.
- [62] G.-S. Jiang, C.-W. Shu, Efficient implementation of weighted ENO schemes, *J. Comput. Phys.* 126 (1996) 202–228.